Version of Record: https://www.sciencedirect.com/science/article/pii/S0921509321015720
Manuscript_381e819a92c3b231304f471f053152a8

Prediction of softening kinetics and recrystallization texture in non-isothermally annealed bulged tubes using CPFEM and CA models

Amir Asgharzadeh[a], Sobhan A. Nazari Tiji[a], Taejoon Park[a], Farhang Pourboghrat[a,b*]

[a] Department of Integrated Systems Engineering, The Ohio State University, 210 Baker Systems, 1971 Neil Avenue, Columbus, OH 43210, United States

[b] Department of Mechanical and Aerospace Engineering, The Ohio State University, 201 W 19th Ave, Columbus, OH 43210, United States

[*] Corresponding author. Tel.: +1(614)292-3124; E-mail: pourboghrat.2@osu.edu

Abstract

A hierarchically coupled cellular automata (CA) model, crystal plasticity finite element method (CPFEM), and thermal finite element (FE) model is developed to predict the softening kinetics of the bulged steel tube during non-isothermal annealing. Through the developed model, the kinetics of softening mechanisms including static recovery (SRV) and static recrystallization (SRX), as well as the recrystallization texture are predicted. Later, the Johnson-Mehl-Avrami-Kohnogorov (JMAK) model based on the predicted SRX data is developed to interpret the recrystallization behavior of the material. To perform this study, diverse experimental tests including tube hydroforming (THF), annealing, uniaxial tensile test, hardness test, as well as microstructure observations through optical microscopy and Electron Backscatter Diffraction (EBSD) tests on steel tube are performed. The obtained experimental data are utilized to calibrate and verify the implemented CPFEM model for simulation of THF process, thermal FE model for prediction of the local temperature over annealing time, and CA algorithm for modeling of the softening kinetics and texture evolution throughout the annealing process. The study shows that the predicted deformation characteristics, softening kinetics, recrystallization texture and temperature profile during non-isothermal annealing are in good agreement with experimental data. During the annealing process, a total of four stages for the kinetics of softening mechanisms is observed: No softening; SRV only; SRV dominant; and SRX dominant. During the progress of SRX, the behavior of recrystallization is abruptly changed, confirming that two different mechanisms are controlling the kinetics of transformation.

Keywords: Tube Hydroforming; Crystal Plasticity Finite Element model; Cellular Automata; Static softening; Recrystallization; texture; JMAK.

1. Introduction

The basics of cellular automata (CA) algorithm for modeling of the recrystallization kinetics was established by Hesselbarth and Göbel [1], where the simultaneous operation of nucleation and grain growth phenomena was assumed to control the progress of recrystallization. Based on the proposed CA algorithm, different CA models have been developed to model the kinetics of recrystallization under complex deformation and annealing conditions. Davies [2] has incorporated the actual microstructure and annealing time into the original CA model to predict

the kinetics of static recrystallization (SRX). Goetz and Seetharaman [3] have implemented different nucleation rules on grain boundaries of a single-phase material to accurately predict the progress of SRX through CA modeling. In their other study [4], the kinetics of dynamic recrystallization and dynamic recovery have been predicted using a CA model. Janssens [5] has implemented the actual space and time coordinates of annealing specimen in a 3D CA model to predict the microstructural changes during recrystallization. Raabe and Hantcherli [6] have considered the effects of deformation texture and Zener pinning in a 2D CA model to describe the kinetics of SRX in a cold-worked interstitial-free steel. In another study, the particle stimulated nucleation model has been incorporated into a CA model to account for the effect of particle stimulated nucleation on the progress of dynamic recrystallization [7]. Kugler and Turk [8] have utilized the actual as-deformed microstructure as the initial state for the CA model to model the kinetics of primary recrystallization. Raabe [9] has developed a modified 3D CA model to obtain crystallographic features of the recrystallized microstructure. Han et al. [10] have implemented nucleation arising from subgrain growth mechanism in a 2D CA model to predict the kinetics of SRX.

Since thermal history and deformation characteristics play an important role in the kinetics of recrystallization, multiple researches have been conducted to incorporate diverse thermal, mechanical, and thermo-mechanical models into the CA model. Yazdipour et al. [11] have developed an irregular CA model to predict the dynamic recrystallization behavior of 304 austenitic stainless steel, in which various thermo-mechanical deformation conditions have been investigated. In another study, the kinetics of SRX in a hot deformed Ni-based superalloy under various thermo-mechanical conditions have been modeled by Lin et al. [12]. In similar studies, the effect of double-pass hot compression tests considering diverse thermo-mechanical conditions on the kinetics of SRX within Al alloys have been investigated through CA simulations by Huang et al. [13] and Zhang et al. [14]. Furthermore, Schäfer et al. [15] have developed a non-isothermal CA model considering the interactive influence of static recovery (SRV) and precipitation on SRX to model the softening kinetics within a cold-rolled Al alloy. Seyed Salehi and Serajzadeh [16,17] have developed a coupled finite element method (FEM) and CA model considering isothermal and non-isothermal annealing conditions to study the effect of rolling process on the subsequent SRX behavior. A similar algorithm has been used by Madej et al. [18] to model the kinetics of SRX within cold-rolled low carbon steel. In addition, Majta et al. [19] have investigated the inhomogeneity of grain topology developed during annealing of as-deformed wires through a coupled FEM and CA model.

Recently, more advanced mechanical models, e.g., crystal plasticity (CP), has been incorporated into CA model to predict the recrystallization kinetics within specimens experiencing complex deformation conditions. Raabe and Becker [20] have developed a coupled crystal plasticity finite element method (CPFEM) and CA algorithm to simulate the behavior of primary recrystallization in a specimen with prior heterogeneous deformation. A similar modeling algorithm has been used by Zheng et al. [21] to model the kinetics of SRX within a hot-compressed low carbon steel. Chuan et al. [22] have implemented a coupled CPFEM and CA algorithm to

model the dynamic recrystallization kinetics of a titanium alloy during isothermal hot compression test. In another study, Popova et al. [23] have developed a coupled CPFEM and CA model to predict the progress of dynamic recrystallization during hot deformation of magnesium alloy. Han et al. [24] have investigated the effect of prior deformation characteristics on the kinetics of SRX using a coupled CPFEM and CA model, in which the subgrain growth mechanism was considered as main nucleation model. Haase et al. [25] have developed a coupled CPFEM and CA model to study the behavior of primary recrystallization within a cold-rolled Twinning-Induced Plasticity steel. Li et al. [26] have developed a fully integrated CPFEM-CA model to investigate the simultaneous interaction of heterogeneous deformation, dynamic recrystallization, and mechanical properties within a hot-worked titanium alloys.

In this study, a coupled CA, CPFEM, and thermal FE model was developed to predict the kinetics of the softening mechanisms during non-isothermal annealing of the bulged steel tubes. As for the experiments, tube hydroforming (THF) tests were performed on low carbon steel tubes using different boundary conditions, and Electron Backscatter Diffraction (EBSD) tests were conducted on the as-received, as-bulged, and subsequently annealed tubes. A rate-independent CPFEM model was developed based on the crystallographic texture of the as-received tube to predict the flow characteristics of the tube under multiaxial loading. Through this modeling, the distribution of stress within the bulged tube was calculated, which then used to estimate the distribution of dislocation density. Furthermore, a thermal FE model was implemented to predict the local temperature within the annealing specimen over annealing time. The grain topology and crystallographic texture of the as-bulged material obtained through EBSD testing, the distribution of dislocation density obtained from CPFEM results, and the distribution of local temperature as a function of annealing time obtained through thermal FE model were collected to create the initial state for the CA model. A CA algorithm comprised of SRV and SRX (nucleation and grain growth) models based on the established initial state for the anneal specimen was developed to predict the kinetics of softening throughout the annealing process. In addition, an algorithm based on the oriented nucleation theory was implemented into the CA model, through which the texture evolution during the progress of recrystallization was predicted. Finally, the Johnson-Mehl-Avrami-Kohnogorov (JMAK) model was derived based on the data extracted from CA simulations to further investigate the progress of recrystallization within the bulged steel tube.

2. Experimental Procedure

In the present study, a low carbon steel tube with the outer diameter and thickness of 38 mm and 1.24 mm, respectively, and chemical composition of Fe - 0.13 wt. %C - 0.3 wt. %Mn - 0.02 wt. %P - 0.15 wt. %Si - 0.3 wt. %S was investigated. The as-received tubes were annealed at 900°C for 75 minutes followed by air cooling to obtain a single phase ferritic initial microstructure. The mechanical properties of these tubes were assessed through uniaxial tensile test based on E8-E8M-09 ASTM standard. A total of five dog-bone specimens with the gauge length and width of 32 mm and 6 mm, respectively, were cut in longitudinal direction of the tube. The uniaxial tensile tests were performed with 3 mm/min grip speed at room temperature. The displacement data

during the tests were recorded using a 3D Digital Image Correlation (DIC) machine, and the synchronized force and displacement data were used to generate engineering strain-stress curves.

The tube hydroforming (THF) tests were carried out with different combinations of axial feed and internal pressure to impose multiaxial loading to the tube. Figure 1 depicts the two different set of boundary conditions employed in this study, which were named "path *A*" and "path *B*". The schematic drawings corresponding to the utilized boundary conditions are shown on the right-hand side of this figure. As illustrated in Figure 1, the axial feed was kept close to zero until 260 s and 277 s of THF process for path *A* and path *B*, respectively. Meanwhile, the internal pressure was linearly increased up to 26 MPa for both deformation paths *A* and *B*. Beyond 260 s of deformation path *A*, a compressive axial feed of 1.65 mm was gradually applied to the tube's end, while the internal pressure was slightly increased to 26.5 MPa until the end of THF process. In contrast, beyond 277 s of deformation path *B*, a tensile axial feed of 1.33 mm and a gradual increase of internal pressure up to 27.6 MPa was applied until the end of THF process. To perform THF tests, the prescribed boundary conditions were precisely applied to the tube using the actuators to apply the axial feed and the intensifier installed in the Interlaken Technology (ITC) machine to apply the internal pressure. Note that the internal pressure was applied through a water pressurization medium. The geometrical characteristics of the tube under hydroforming including biaxial strain components were recorded using a DIC equipment throughout the bulging process. The details of the procedure utilized to perform THF process were explained in the authors' previous papers [27–29].

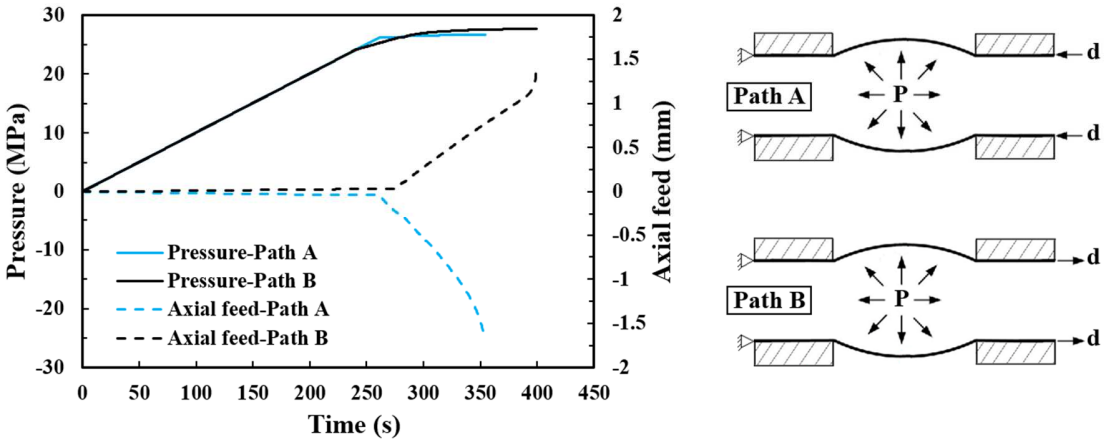

Figure 1: The utilized boundary conditions for THF process, including the internal pressure (P) and axial feed (d), along with their corresponding schematic drawings.

Subsequently, the as-deformed tubes were annealed in a furnace preheated to the temperature of 960 K under different heating rates. Different ambient environments inside the furnace were designed to create diverse heating rates in the anneal samples. The temperature change within the bulged specimen during the annealing process was recorded using a K-type thermocouple, which was attached to the specimen through a hole drilled through the thickness of the specimen [30].

Following the annealing process, each specimen was quenched in cold water to preserve the final microstructure. Then, the hardness measurements were performed on all specimens to assess the changes in mechanical properties of the specimens during the annealing treatment. In order to accommodate for the curvature of the bulged specimens, the convex surface of the specimen was placed on the flat holder, and the concave side of the sample was penetrated by the spherical indenter of Rockwell hardness machine [31].

The microstructural observations have been performed on the as-received, as-deformed, and annealed specimens through optical microscope (OM) and electron backscatter diffraction (EBSD). The deformed and annealed specimens were cut along the hoop direction at the pole of the bulged tubes where the maximum deformation occurred. Then, all the samples were mounted and polished up to 0.05 μm roughness. To observe the grain topology with OM, all the samples were etched by Nital detergent containing 100 ml ethanol and 5 ml nitric acid. Furthermore, the crystallographic texture of the samples were measured by means of a ThermoScientic™ApreoLoVacfield emission EBSD microscope equipped with EDAX Hikari XP camera [32].

3. Modeling Methodology

3.1. Crystal Plasticity (CP) model

In this study, a rate-independent CP model is employed to simulate the THF process within steel tubes. The present CP model was first implemented by Zamiri and Pourboghrat [33] to model the evolution of anisotropic plasticity of a single-phase Al tube. Later on this model was adopted to capture the plasticity of advanced multiphase materials [34–36], as well as virtual testing of materials by constructing 3D representative volume element (RVE) for calibration of advanced yield functions and modeling of advance manufacturing processes [36–38]. The fundamentals of the utilized model are briefly presented in this section.

In the present CP model [33], the yield function, $f(\sigma, q)$, for a single crystal is defined as follows,

$$f(\sigma, q) = \frac{1}{\rho} ln\left\{\sum_{\alpha=1}^{N} exp\left[\rho\left(\frac{|\sigma:P^{\alpha}|}{\tau_y^{\alpha}} - 1\right)\right]\right\} \quad (1)$$

where α, N, and τ_y^{α} denote the slip system, the number of slip systems, and the critical resolved shear stress (CRSS), respectively. In addition, ρ is a parameter to determine the closeness to the condition, $|\sigma: P^{\alpha}| = \tau_y^{\alpha}$, and P^{α} is the Schmid tensor describing the orientation of a slip system. To account for the increase of the current slip resistance against shear stress (τ_y^{α}) in comparison to the initial critical resolve shear stress (τ_0^{α}) due to hardening effect, the following hardening equation is employed:

$$\dot{\tau}_y^{\alpha} = \sum_{\beta=1}^{N} h^{\alpha\beta}\left|\dot{\gamma}^{\beta}\right| \quad (2)$$

where $\dot{\gamma}^{\beta}$ is the shear slip rate and $h^{\alpha\beta}$ are denoted as the components of the hardening matrix. The hardening matrix can be defined based on the model proposed by Hutchison [39] as follows,

$$h^{\alpha\beta} = h^{\beta}\left[q + (1-q)\delta^{\alpha\beta}\right] \quad (3)$$

where q is the latent hardening ratio with values in the range of $1 < q < 1.4$, and h^{β} is an evolutionary function denoting the self-hardening rate, which can be expressed as [40],

$$h^{\beta} = h_0 \left| 1 - \frac{\tau_y^{\beta}}{\tau_s} \right|^{a_0} . sgn\left(1 - \frac{\tau_y^{\beta}}{\tau_s} \right) \quad (4)$$

where h_0, τ_s, and a_0 are the hardening parameters, denoting the initial hardening rate, the saturation value of the slip resistance, and the exponent describing the shape of the function, respectively.

In the present CP model, the Taylor type homogenization is adopted to calculate the homogenized stress for each integration point. In this approach, multiple grains are assigned to each integration point in the finite element (FE) simulation, and each grain undergoes the same deformation condition applied to the integration point. In this study, by assuming the same grain volume (V^c) for all grains for the sake of simplicity, and based on the crystal stress (σ_c) calculated for each grain, the homogenized stress can be determined by,

$$\langle \sigma \rangle = \frac{V^c}{V^G} \sum_c \sigma_c = \frac{1}{M^G} \sum_c \sigma_c \quad (5)$$

where V^G and M^G are the total volume of grains, and the number of grains, respectively [40].

3.2. Thermal FE model

As temperature is one of the key factors controlling the kinetics of softening mechanisms, development of an accurate thermal model to predict the variation of temperature during the annealing process is crucial. Therefore, in the present study, a thermal model is hierarchically coupled with the cellular automata (CA) model to account for the temperature gradient throughout the annealing process. In this regard, a three-dimensional transient thermal FE model is developed to determine the local temperature gradient within the bulged specimen during the annealing process. The governing heat conduction equation in the Cartesian coordinate system can be expressed as [16]:

$$\frac{\partial}{\partial x}\left(\Lambda \frac{\partial T}{\partial x} \right) + \frac{\partial}{\partial y}\left(\Lambda \frac{\partial T}{\partial y} \right) + \frac{\partial}{\partial z}\left(\Lambda \frac{\partial T}{\partial z} \right) = \rho_m c \frac{\partial T}{\partial t} \quad (6)$$

where Λ, ρ_m, and c are the coefficient of heat conduction, material density, and specific heat, respectively. In addition, the following boundary condition is applied to all the specimen surfaces exposed to the high temperature environment [30],

$$\Lambda \left(\frac{\partial T}{\partial \xi} \right)_{\Gamma} + h(T - T_{stablized}) = 0 \quad (7)$$

where ξ is the normal direction to every surface boundary Γ, and h and $T_{stablized}$ are the heat transfer coefficient and furnace stabilized temperature, respectively. In the present study, the thermal model coefficients are defined as temperature dependent functions to improve the accuracy of predictions. These functions for low carbon steel are listed in Table 1.

Table 1: The properties of low carbon steel required for thermal model [41].

Parameters	Temperature dependent function (in K)
Material density ($kg.m^{-3}$)	7800
Specific heat ($J.kg^{-1}.K^{-1}$)	284.7217+0.5051×T
Thermal conductivity ($W.m^{-1}.K^{-1}$)	114.6667-0.0917×T; if T<900 33; if T≥ 900

3.3. Modeling of softening kinetics and texture evolution

3.3.1. Recovery

Recovery phenomenon generally occurs during annealing of deformed materials with high stacking fault energy. To predict the softening kinetics during annealing, the simultaneous contributions of SRV and SRX in restoration should be determined. In this regards, the kinetics of SRV during post-deformation annealing can be estimated by the analytical approach proposed by Verdier et al. [42]. According to this model, the relaxation of internal stresses and annihilation of dislocations caused by thermally activated mechanisms are the main consequence of recovery. Therefore, the relaxation of internal stress during recovery can be derived as [42],

$$\frac{d\langle\sigma\rangle}{dt} = -\frac{E\rho_d b^2 \nu_D}{M_\alpha}\, exp\left(\frac{-Q_r}{RT}\right)\, sinh\left(\frac{\langle\sigma\rangle\omega}{kT}\right) \quad (8)$$

where E, t, R, Q_r, T, ν_D, ω, k, and M_α are Young's modulus, annealing time, universal gas constant, recovery activation energy, temperature, Debye frequency, recovery activation volume, Boltzmann constant, and Taylor factor, respectively. The dislocation annihilation rate ($\dot{\rho_d}$) during static recovery can be estimated by applying chain rule to Eq. (8) and employing Taylor model, as below [17]:

$$\dot{\rho_d} = \frac{d\rho_d}{d\langle\sigma\rangle}\frac{d\langle\sigma\rangle}{dt} = -\frac{4(1+\nu)\rho_d{}^{1.5} b\nu_D}{\lambda {M_\alpha}^2}\, exp\left(-\frac{Q_r}{RT}\right) sinh\left(\frac{\lambda M_\alpha G b\sqrt{\rho_d}\omega}{kT}\right) \quad (9)$$

where ν is Poisson's ratio, and λ is a constant. Using this equation, the local dislocation density can be modified during the annealing process as a function of annealing duration and temperature based on a step-size adjustment method. This method will be explained in the upcoming sections.

3.3.2. Grain growth

The progress of SRX is generally identified by simultaneous occurrence of nucleation phenomenon as the formation of defect-free nuclei, followed by their growth toward the neighboring deformed region. Both mechanisms are basically controlled by the amount of stored internal energy during deformation as well as the temperature regime during subsequent annealing process. In the CA model, the growth mechanism can be interpreted by the term of local velocity of grain boundary (V), which can be defined based on the Turnbull's rate equation [43] for the grain boundary between recrystallized and unrecrystallized grains,

$$V = M.P \quad (10)$$

where P is the local driving pressure, and M is the local mobility of grain boundary that can be calculated for ferritic grain boundaries in a low carbon steel as follows [44],

$$M = \frac{5.4\times10^{-8}b}{kT} exp\left(-\frac{Q_m}{RT}\right) exp\left(-\frac{Q_{gb}^{\alpha}}{RT}\right) \quad (11)$$

where Q_m and Q_{gb}^{α} are the activation energies for the grain boundary motion and the grain boundary diffusion, respectively. In addition, the following relationship can be used to calculate the local driving pressure (P) existing on a moving grain boundary,

$$P = \lambda G b^2 \Delta\rho_d + \kappa\gamma_{GB} \quad (12)$$

where $\Delta\rho_d$ is the change in dislocation density over the moving grain boundary, and γ_{GB} and κ are the grain boundary energy and curvature, respectively. In the present model, the kink-template method [10] is employed to approximate the grain boundary curvature (κ). Furthermore, the Read-Shockley equation [17] is utilized to calculate the energy of grain boundary (γ_{GB}) as follows,

$$\gamma_{GB} = \begin{cases} \gamma_{HAGB}\frac{\Delta\theta_{AB}}{\Delta\theta_{HAGB}}\left(1 - ln\left(\frac{\Delta\theta_{AB}}{\Delta\theta_{HAGB}}\right)\right) & if \ \ \Delta\theta_{AB} < \Delta\theta_{HAGB} \\ \gamma_{HAGB} \quad if & \Delta\theta_{AB} \geq \Delta\theta_{HAGB} \end{cases} \quad (13)$$

where $\Delta\theta_{AB}$ is the grain boundary misorientation, $\Delta\theta_{HAGB}$ is the misorientation on a high angle grain boundary (=15°), and γ_{HAGB} is the energy of high angle grain boundary.

In the CA model, the actual annealing time is discretized into multiple time steps, in which the grain growth phenomenon is assumed to occur in a stable manner. Therefore, the simulation time step (Δt) is calculated using the following relationship:

$$\Delta t = \frac{l}{V_{max}} \quad (14)$$

where V_{max} is the maximum velocity of grain boundary obtained from Eq. (10).

3.3.3. Nucleation

The nucleation phenomenon is the formation of defect-free nucleus on the high energy spots of the deformed context. The kinetics of nucleation phenomenon during SRX is basically dependent on the temperature and the amount of energy reduction due to the occurrence of nucleation. Therefore, the nucleation rate ($\dot{n}$) is calculated as below [27],

$$\dot{n} = c_0 \Delta\Sigma \, exp\left(\frac{-Q_N}{RT}\right) \quad (15)$$

where c_0 and Q_N are a positive fitting factor and the nucleation activation energy, respectively. In addition, $\Delta\Sigma$ is the magnitude of energy change during nucleation, which can be calculated through the following relationship:

$$\Delta\Sigma = \lambda V_n G b^2 \Delta\rho_d + \sum A_{GB}\gamma_{GB} \quad (16)$$

where V_n and A_{GB} are the volume of nucleus and area of grain boundary, respectively. In this relationship, the first term takes the energy change due to the reduction of dislocation density into account, in which the magnitude of $\Delta\rho_d$ is defined as the difference between dislocation density of the site and dislocation density of the annealed structure. In addition, the second term is the total surface energy change due to nucleation, which is the summation of energy reduction due to the removal of prior grain boundaries and energy increase due to the formation of new grain boundaries.

Based on the nucleation rate calculated through Eq. (15), the local nucleation probability for the time increment i is determined as follows,

$$P^{i}_{nucleation} = \dot{n}^{i} l^{3} \Delta t_{i} \quad (17)$$

In this equation, the value of Δt_i is determined by Eq. (14). It is important to note that the fresh crystals are assumed to be nucleated at preferred high energy spots such as triple junctions and grain boundaries, since it is reported that heterogeneous nucleation takes place within samples with a slight imposed strain [45]. Therefore, the probability of nucleation calculated for each preferred nucleation site throughout the microstructure is compared to a pseudorandom number, generated through Mersenne-Twister algorithm [46], to decide whether the transformation from deformed site into a recrystallized fresh nucleus can occur.

3.3.4. Modeling of texture evolution

The softening mechanisms operative during the annealing process may lead to texture evolution in metallic materials. The texture change through softening mechanisms may vary from absolutely none to drastic evolutions. It is known that SRV could contribute to the texture evolution through formation of subgrain structure, while SRX may cause the texture evolution by forming fresh crystals from the strained context. Regarding the SRX phenomenon, the combination of different nucleation parameters including the orientation of fresh nuclei, the location of fresh grains, and the stored energy within the surrounding grains as well as the subsequent growth rate are influential on the development of recrystallization texture [47].

Because of the mutual interaction between the softening kinetics and texture evolution throughout the annealing process, it is important to model both phenomena interactively in the developed CA model. In the previous section, the impact of the grain orientation was incorporated into the nucleation and grain growth algorithms through its effect on the energy of grain boundary (see Eq. (13)). Herein, an algorithm based on the oriented nucleation theory [48] is developed to model the texture evolution during the annealing process. Note that the impact of the subgrain formation through SRV on the texture evolution is neglected in the present study since not only this impact is negligible but also the CA cell resolution is not sufficiently high to be able to account for the subgrain structure [27]. According to the oriented nucleation theory, a specific set of orientations may have higher chance to nucleate during recrystallization. These orientations eventually become the dominant recrystallization orientations toward the end of the annealing process that may define the final texture distribution and intensity [48,49]. Through this model, a new orientation is assigned to the freshly nucleated grain, which is subsequently reproduced in the recrystallized cells during grain growth.

Relying on the oriented nucleation theory, three different algorithms are proposed in the present study to assign new orientations to the fresh nucleus, which may describe the recrystallization texture evolution during annealing of low carbon steel:

i) *Unchanged Orientation*: in which the orientation of the fresh nucleus is kept unchanged after transformation to the recrystallization state,

ii) *Average Orientation*: in which the orientation of the new nucleus is defined by averaging the orientations of the surrounding grains based on the vector addition theorem,

iii) *Random Orientation*: in which a random orientation is assigned to the fresh nucleus.

This algorithm may not effectively predict the severe texture evolutions during annealing of the materials in which a new preferred orientation is developed during recrystallization phenomenon. However, it can successfully describe the recrystallization texture in materials with either slight changes in orientation distribution or significant texture evolutions toward the randomized orientations during the annealing process.

3.4. Hierarchical coupling of CP, FE and CA models

It is well established that the kinetics of softening phenomena is significantly affected by the prior deformation characteristics as well as the subsequent thermal regime during the annealing process. Therefore, in this study, a hierarchically coupled CPFEM and CA model along with a thermal FE model is implemented to model the softening kinetics, including SRV and SRX, as well as the developed texture during the annealing of bulged steel tube under the non-isothermal annealing condition. Afterwards, the JMAK model is derived based on the recrystallization data attained through the CA model to interpret the SRX behavior throughout the annealing process. It should be mentioned that the formation of second phase particle during annealing of steels is quite common, which can interfere with the progress of softening phenomena that is called Zener-type particle pinning [6]. As Raabe and Hantcherli [6] have reported, the impact of Zener-pinning on the kinetic of recrystallization within steels with a low volume fraction of the second phase particles is insignificant. Therefore, the Zener-pinning effect is neglected in the present study since the volume fraction of second phase particles is negligible.

The macro-level flowchart of the developed algorithm to model the softening kinetics during the non-isothermal annealing process is depicted in Figure 2-a. The modeling procedure in the present study is explained below:

a) The THF process on the steel tube is performed at room temperature (section 2).

b) Experimental and numerical material characterization procedures are adopted to analyze the state of material at the as-deformed condition. Therefore, the prior deformation characteristic is obtained through CPFEM modeling (section 3.1), while the as-deformed microstructural data are extracted from EBSD maps collected from the specimen (section 2) and analyzed by MATLAB toolbox MTEX [50].

c) The as-deformed state of the material as initial state for the CA model is constructed based on the data from step (b), including prior deformation properties such as dislocation density and specimen geometry, as well as the tube's as-deformed microstructural data such as grain topology and crystallographic texture. Then, all the information is assigned to a spatial region called cell structure and directly used as input to the CA model.

d) The thermal FE model (section 3.2) and CA algorithm (section 3.3) based on the material's as-deformed geometry and CA initial-state are solved integratively. Figure 2-b shows the detailed procedure of this solution, while the step-by-step approach is explained as follows,

i) The CA time increment (Δt) is defined through Eq. (14), in which V_{max} is obtained based on the local grain boundary velocities calculated by Eq. (10) at previous time increment;

ii) The annealing time ($t = t_0 + \Delta t$) is updated and the local temperature gradient within the bulged specimen is determined through the thermal FE model (section 3.2);

iii) The temperature field at time t is compared to the temperature field at time t_0 to check if the temperature change during the time increment Δt in the solution domain (ΔT_{max}) is larger than a predefined critical value ($\Delta T_{cr} = 0.5$ K). In the case of large temperature gradient over Δt, the solution time increment is refined as follows:

$$\Delta t_{new} = \frac{\Delta T_{cr}}{\Delta T_{max}} \Delta t \quad (18)$$

Therefore, the CA model time (t) is modified according to the refined time increment (Δt_{new}) and the temperature field is updated through linear interpolation of the obtained thermal data;

iv) Based on the temperature field obtained for the annealing specimen, the dislocation density assigned to each spot at cell structure is updated through the recovery model (section 3.3.1).

v) The value of $P_{nucleation}$ for each preferred nucleation site is calculated using Eq. (17), and the probability of grain growth ($P_{growth} = V/V_{max}$) for each cell on the boundary of recrystallized and unrecrystallized regions is calculated using data from Eq. (10) (sections 3.3.2 and 3.3.3).

vi) The nucleation and grain growth probability values are compared to pseudorandom number to decide whether the transformation can take place.

vii) The cell information including recrystallization state, dislocation density, and orientation (section 3.3.4) is updated based on the decisions made in step (vi).

e) The JMAK model is developed based on the recrystallization data attained through CA model throughout the annealing process to interpret the behavior of SRX at every stage of the annealing process.

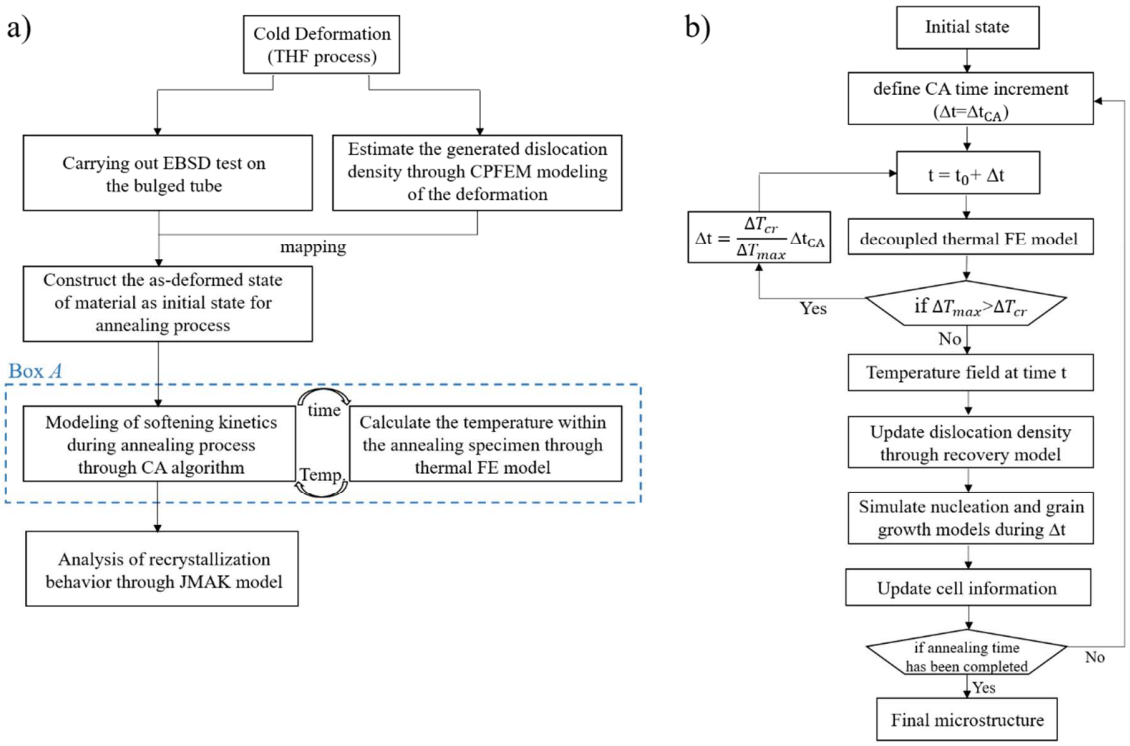

Figure 2: a) Macro-level flowchart of the developed algorithm for modeling of softening phenomena under non-isothermal condition, and b) a step-by-step integrative solution for thermal FE and CA models corresponding to Box *A* in part (a).

4. Model Calibration

4.1. CP model calibration

To obtain the model parameters defined in crystal plasticity algorithm, the CP model is calibrated against the experimental uniaxial tensile test data through performing tensile test simulations in the ED direction of the as-received material. To that end, the crystallographic texture of the as-received steel tube is obtained by means of EBSD testing. The EBSD map as well as the pole figure (PF) of the as-received steel tube collected from the hoop cross-section is shown in Figure 3. As seen in Figure 3-a, the initial microstructure is mainly comprised of equiaxed grains with some grains slightly elongated toward extrusion direction (ED) because of the prior production procedure. In addition, the PF of the as-received material shown in Figure 3-b confirms the presence of multiple preferred texture components within the steel tube, which may significantly affect the subsequent deformation characteristics.

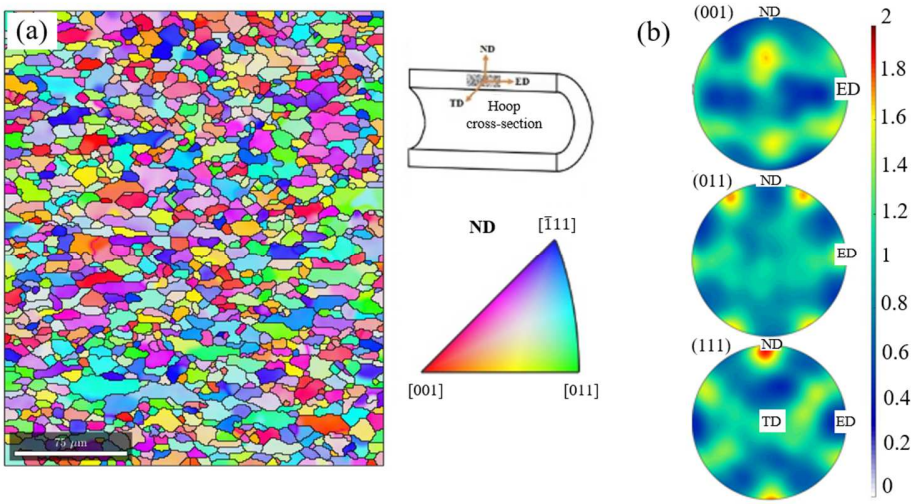

Figure 3: a) EBSD map, and b) pole figure collected from the hoop cross-section of as-received steel tube.

The CP model parameters are obtained by performing virtual tensile test in the ED direction of the as-received material based on CPFEM algorithm. In this regard, a representative volume element (RVE) is created by Dream 3D software and the extracted grain orientations from EBSD maps are assigned to its elements. It is assumed that each element within the RVE represents 50 equally sized grains with their crystal orientation information. Furthermore, it is assumed that the 12 slip systems of {110}<111> and 12 slip systems of {112}<111> out of total 48 slip systems available in BCC crystals are activated during deformation. The created RVE for calibration of CP model as well as the applied boundary condition is illustrated in Figure 4-a. As can be seen, symmetry boundary conditions are applied to three adjacent surfaces of the RVE, while a displacement boundary condition is defined on the opposite surface along ED. The dimension of this RVE is 20 μm ×20 μm ×20 μm and the element size is 1 μm. The comparison between the engineering strain-stress curves obtained from CPFEM simulation after the calibration and experimental uniaxial tensile test in ED of the tube is shown in Figure 4-b. As can be seen, the CPFEM prediction matches the experimental data very well using the material constants and model parameters listed in Table 2. It should be noted that among the parameters listed in Table 2, only τ_y^0, h_0, and τ_s are used for calibration of CP model against experimental tensile data, while the rest of parameters are obtained from literature as material constant [36,51,52].

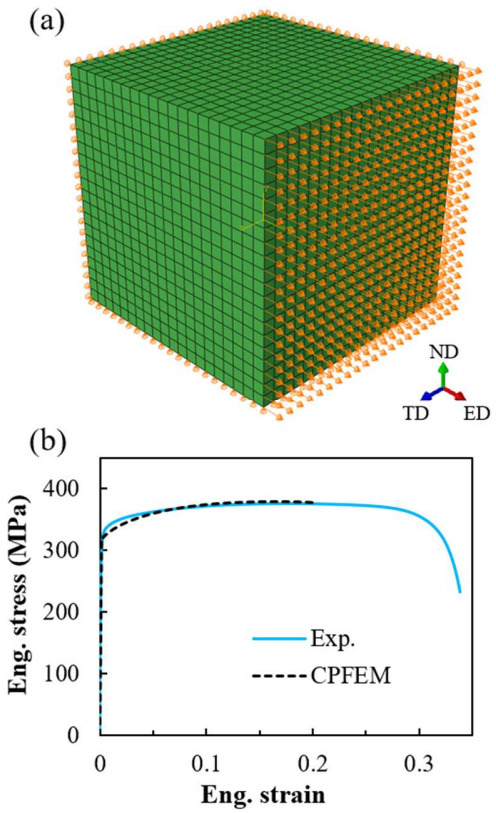

Figure 4: (a) The created RVE for calibration of CP model, and (b) the experimental uniaxial tensile behavior of as-received material along ED compared to the CPFEM prediction.

Table 2: The calibrated material constants and model parameters used for CPFEM model [36,51,52].

Type	c_{11} (GPa)	c_{12} (Gpa)	c_{44} (Gpa)	a_0	q	τ_y^0 (Mpa)	h_0 (Mpa)	τ_s (Mpa)
BCC	231	135	116	2	1.4	143	680	250

4.2. Thermal FE model calibration

In the present study, a transient thermal FE model, as explained in section 3.2, is adopted to determine the temperature gradient within the bulged specimen during the annealing process. To solve the thermal problem, the described thermal model is implemented through the commercial Abaqus/Heat transfer FE code. To that end, a strip of the bulged tube's geometry in longitudinal direction is established in three-dimensional space (see *Appendix A-A1*). The specimen is discretized into 29600 equal sized 0.31 mm × 0.31 mm × 0.31 mm eight-node linear heat transfer brick element with reduced integration (DC3D8R).

To examine the influence of non-isothermal annealing on the kinetics of softening phenomena within bulged specimens, the samples are annealed under different ambient conditions. For each ambient condition, the predicted temperature gradient is calibrated with respect to the recorded temperature history to obtain the corresponding heat transfer coefficient (h). Figure 5 shows the comparison between the predicted and the experimental temperature history during the annealing

of bulged specimens at temperature of 960 K under diffident ambient conditions. A good agreement is observed between the experimental and the predicted temperature history, in which the heat transfer coefficient is found to vary between 20 to 125 W/m.K. As shown, increasing the heat transfer coefficient would result in a rapid temperature rise at early stages of the annealing process, which makes the annealing condition very close to the isothermal assumption.

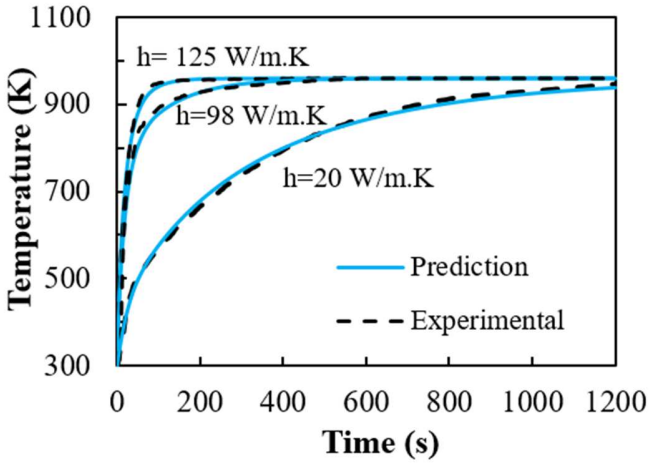

Figure 5: The comparison between the predicted and experimentally recorded temperature history throughout the annealing process at temperature of 960 K under different heating rates.

4.3. CA model calibration

As previously explained, numerous model parameters are defined in the CA algorithm to properly simulate the kinetics of recovery, nucleation, and grain growth. To identify these parameters, a set of experimental data is taken as the reference data, and multiple CA simulations are performed to precisely calibrate the model parameters against the reference data. Thereafter, the obtained parameters are used to model the remaining annealing experiments to validate the accuracy of the model.

As the first step for CA simulations, the initial state of the annealing specimen should be defined. To that end, EBSD tests on as-deformed specimen is performed to obtain the microstructure and crystallographic texture data. Thereafter, the grain topology information as well as the Euler angles extracted from EBSD data are mirrored to a grid structure called cell structure, which is compatible with our in-house CA code.

The EBSD maps collected from the hoop cross-section of the as-deformed materials bulged through deformation paths *A* and *B* are shown in Figure 6. The EBSD data are collected from a region approximately located on the pole of the bulged tube, as schematically illustrated in Figure 6. As can be seen, the microstructure of bulged tubes deformed through path *A* and path *B* mainly consist of fine grains, which are slightly elongated toward the extrusion direction (ED). In addition, an inhomogeneous distribution of grain orientations within the microstructures is observed, which results in a varying grain boundary energy throughout the microstructure leading to

inhomogeneous nucleation and grain growth. It is reported that in materials with preferred texture, the inhomogeneity of energy between grain boundary and inside the grain may become stronger due to the accumulation of dislocations at grain boundaries [27,45]. Therefore, the triple junctions and grain boundaries are defined as the preferred nucleation and growth sites in this study.

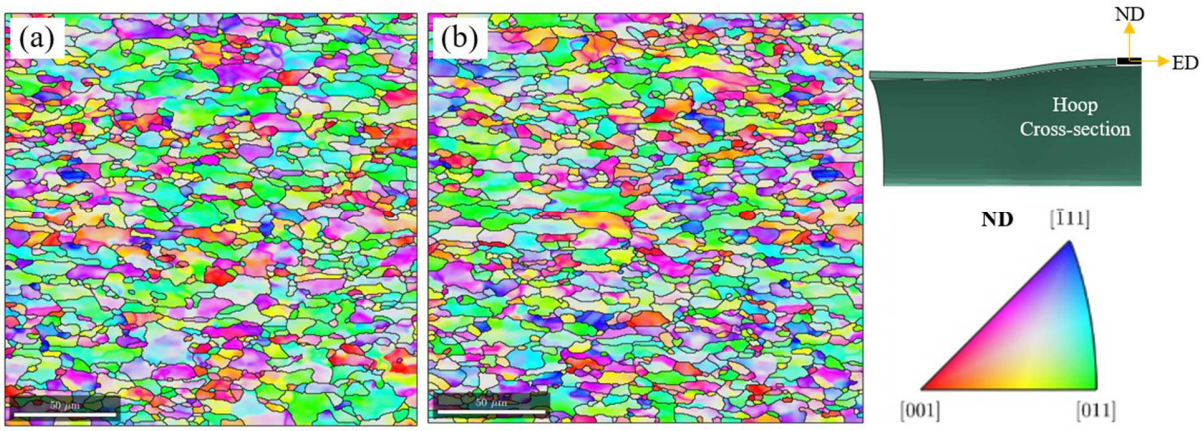

Figure 6: EBSD map collected from the pole of as-bulged tube through a) path *A*, and b) path *B*.

The set of experimental data employed to calibrate the CA model parameters is shown in Figure 7, which are obtained from specimen deformed through path *B* and annealed at T=960 K, h=125 W/m.K, and different durations. The experimental microstructures obtained from the as-bulged, partially recrystallized, and fully recrystallized samples are shown in Figures 7-a, -b, and -c, respectively. The corresponding predicted microstructures by the calibrated CA model are illustrated in Figures 7-d to -f, in which the grains (shown with different random colors) are distinguished by their crystal orientation. Figure 7-d represents the as-bulged tube's microstructure at the pole of the tube undergone deformation path *B*, which is generated by mapping the grain topology and orientation data of the EBSD map illustrated in Figure 6-b. In addition, the CA model parameters obtained through the calibration process along with the material properties for low-carbon steel are listed in Table 3 [27,44,53]. The comparison of the microstructures for partially and fully recrystallized specimens shows a reasonable agreement between the experimental and predicted results in a qualitative manner.

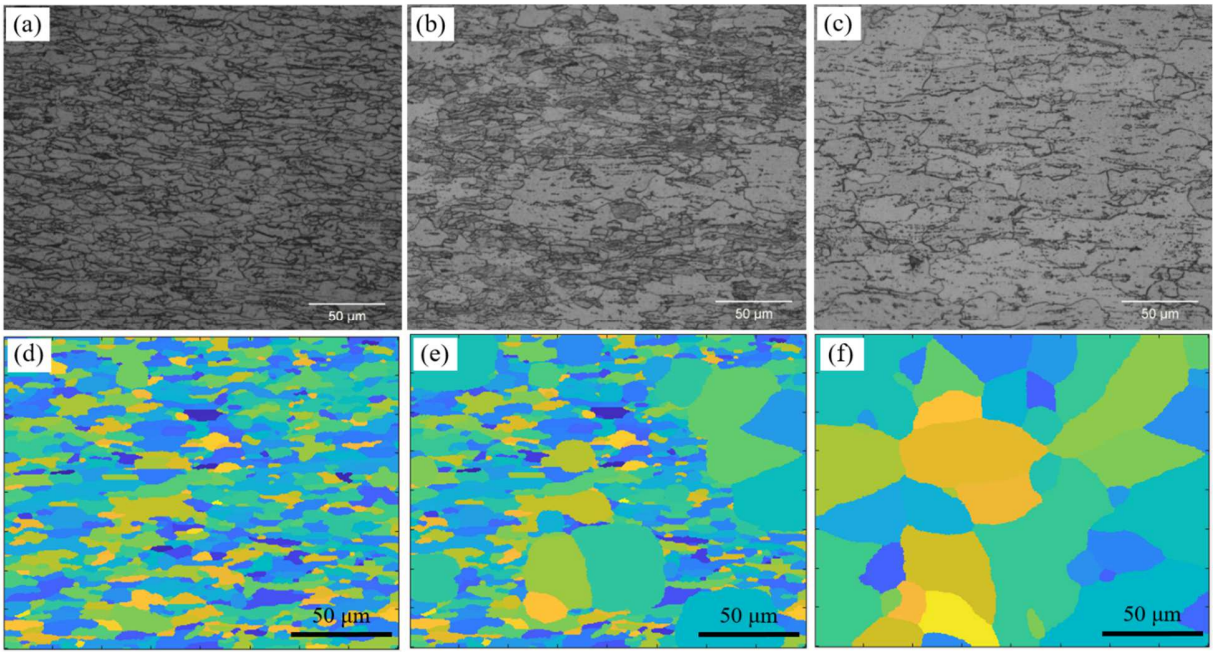

Figure 7: The comparison between the experimental (a-c) and predicted (d-f) microstructures during annealing of bulged specimen deformed under path *B* and annealed at T=960 K, h=125 W/m.K, and duration of (a, d) 0 s, (b, e) 120 s, and (c, f) 180 s.

Table 3: The properties of low carbon steel required for CA model [27,44,53].

Parameters	λ	M_α	ν	b (m)	γ_{HAGB} (J/m^2)	G (GPa)	E (GPa)
Value	0.5	3	0.3	2.48×10^{-10}	0.56	69.3	200
Parameters	Q_m (kJ/mole)	Q_N (kJ/mole)	Q_{gb}^{α} (kJ/mole)	Q_r (kJ/mole)	ν_D (Hz)	ω (m^3)	
Value	151.4	140.2	123	345	2×10^{12}	36 b^3	

During the calibration process, considering a quantitative approach to better understand the accuracy of the predictions is of great importance. In this regard, the experimental and predicted grain size distribution of the specimens throughout the annealing process are compared in this study. To that end, the CA simulation for each annealing condition is repeated for at least five times and the average grain size distribution along with the corresponding standard deviation is considered as the simulation result. The reason is that the CA model is basically a probabilistic algorithm that may cause a minor variation in simulation results among different repeats. Figure 8 depicts the comparison between the grain size distributions obtained from experimental observations and CA simulations corresponding to the microstructures shown in Figure 7. As can be seen, there is a tight agreement between the experimental and predicted grain size distribution

of the partially recrystallized (Figure 8-b) and fully recrystallized (Figure 8-c) specimens with a corresponding average root mean square error [54] of 1.5 % and 2.2 %, respectively.

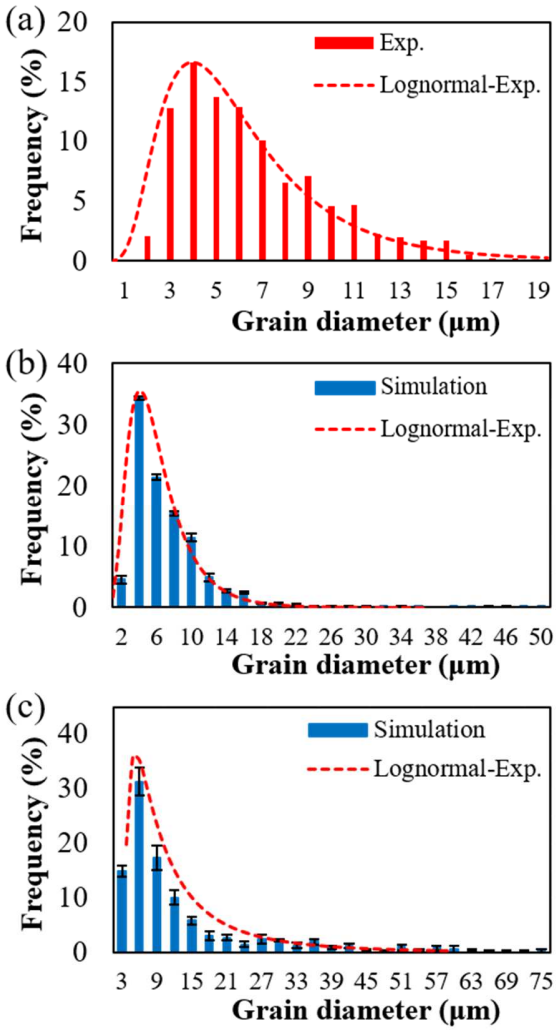

Figure 8: The comparison between predicted and experimental grain size distribution of partially and fully recrystallized specimens deformed under path *B* and annealed at T=960 K, h=125 W/m.K, and duration of (a) 0 s, (b) 120 s, and (c) 180 s.

5. Results and Discussion

5.1. Mechanical modeling of THF process

To model the THF process, the described polycrystal CP model with the material properties provided in Table 2 is incorporated into the commercial Abaqus/Explicit finite element code using the user-defined material subroutine VUMAT. In this model, a fixed mass scaling factor of 10^{12} is applied to reduce the computational time. For the simulation, a FE model considering $1/8^{th}$ of the

tube's geometry with thickness of 1.24 mm and outer diameter of 38 mm is established in three-dimensional space. To apply the prescribed boundary conditions on the tube, the time dependent axial displacement and internal pressure profiles (Figure 1) are applied to the outer end of the tube and the tube's interior surface, respectively. The established FE model for mechanical simulation of THF process can be seen in *Appendix A-A2*. Like the schematic drawings in Figure 1, in the established FE model, one end of the tube is encastered along ED, while the opposite end is free to move only in ED (one degree of freedom). In addition, symmetry boundary conditions are applied to all the cut edges in three principal directions. Furthermore, a uniform distribution of the internal pressure is applied to the entire internal surface of the tube.

Since the plastic strain within the bulged tube is localized at the mid cross-section (pole of the tube), the arrangement of meshes is defined in a way that they gradually become finer from $1.1 \times 0.42 \times 0.31$ mm^3 on the edge to $0.2 \times 0.42 \times 0.31$ mm^3 when getting closer to the mid cross-section of the tube (see *Appendix A-A2*). This arrangement of meshes improves the accuracy of stress and displacement field predictions throughout the bulged tube. In this study, the eight-node linear brick element with reduced integration (C3D8R) is defined for the tube, and four elements are considered through the thickness to precisely capture the deformation gradient in thickness direction.

The comparison between the distribution of major logarithmic strain in the bulged tube obtained through DIC measurement and CPFEM simulation is shown in Figure 9. As depicted, a non-uniform distribution of logarithmic strain in the longitudinal direction is observed with the maximum strain occurring at the pole of the tube where the bulge height is maximum. Note that the simulation results depicted in Figures 9-b and -d correspond to the $1/8^{th}$ of the tube's geometry, in which the pole of the bulged tube is located on the left-hand side of the figures. In addition, the maximum major logarithmic strain for path *A* and path *B* obtained via DIC measurement is 0.142 and 0.179, and via CPFEM simulation is 0.144 and 0.171, respectively. Also, the distribution of major strain obtained through DIC measurement and CPFEM simulation are quite similar.

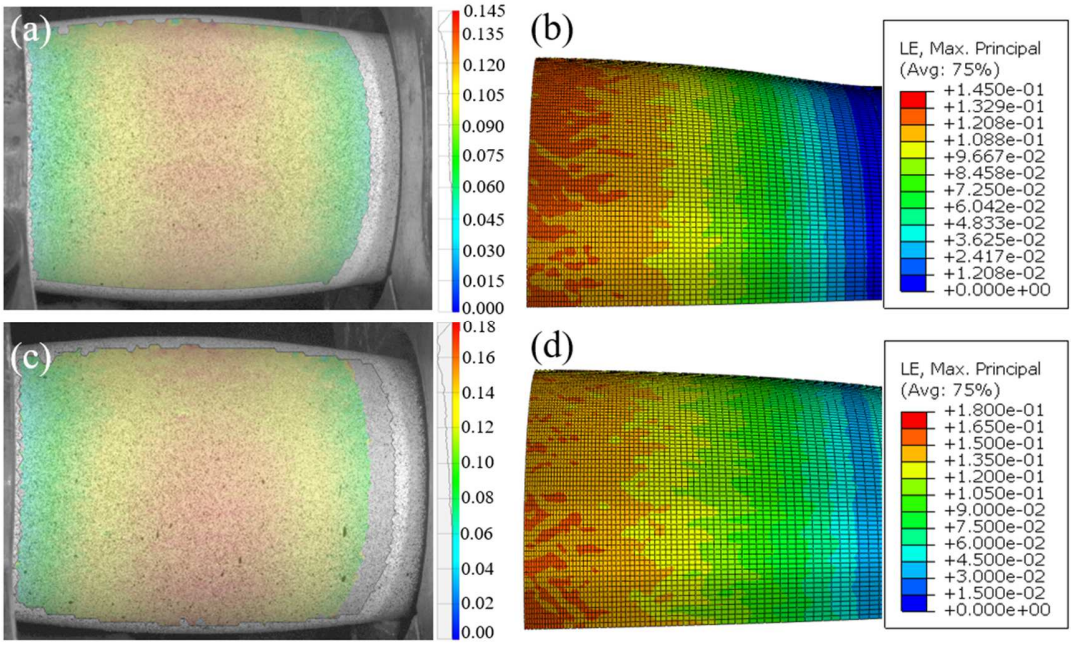

Figure 9: The comparison of the distribution of major logarithmic strain between DIC measurement (left) and predicted CPFEM simulation (right) for deformations (a-b) path *A*, and (c-d) path *B*.

To quantify the accuracy of CPFEM modeling results, the predicted multiaxial flow characteristics of the bulged tubes are compared to the experimental results. To that end, an analytical solution is derived to determine the principal strain and stress components at the pole of the bulged tube from the displacement data measured by DIC technique. The detailed formulation for this approach is provided in *Appendix B*, which can also be found in ref. [27,28]. Figure 10 compares the principal components as well as the equivalent flow curve calculated through the analytical solution based on the DIC data and with those obtained from the CPFEM modeling. As can be seen, a reasonable agreement between the flow curves obtained through DIC data and predicted by the CPFEM modeling is achieved.

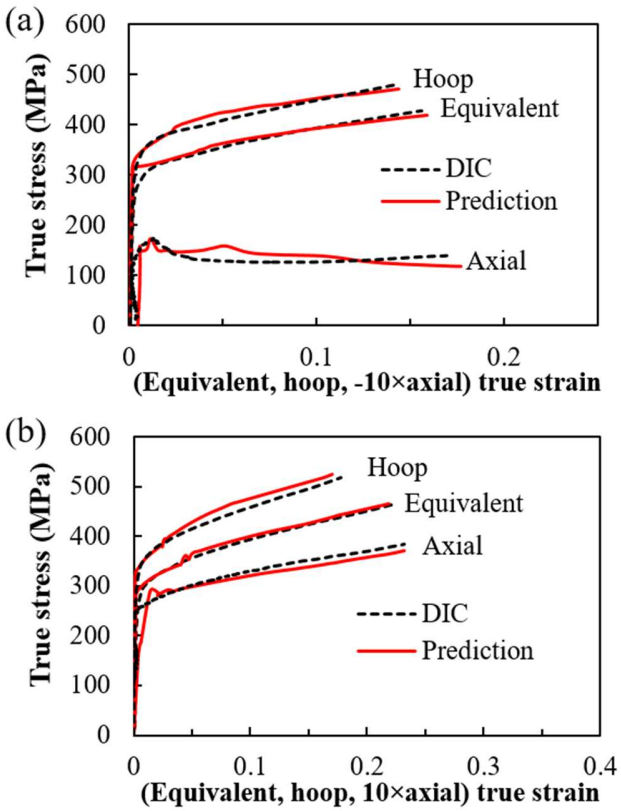

Figure 10: The comparison of experimental and CPFEM predicted flow behavior of THFed specimens deformed under (a) path *A*, and (b) path *B*.

To connect the deformation characteristics of THF process to the microstructural events happening during subsequent annealing process, the equivalent stress at the last time increment of THF is used to estimate the amount of dislocation density generated during deformation. Therefore, the local dislocation density (ρ_d) at each element is calculated through the following relationship [42]:

$$\rho_d = \left(\frac{\langle\sigma\rangle}{\lambda M_\alpha G b}\right)^2 \tag{19}$$

where M_α, λ, b, and G are Taylor factor, a constant, burgers vector, and shear modulus, respectively.

5.2. Modeling of the softening kinetics within bulged steel tube

The microstructure-based CA model hierarchically coupled with CPFEM, and thermal FE models is developed to predict the kinetics of softening mechanisms including SRV and SRX during non-isothermal annealing of the bulged tubes. In most of the metallic materials, SRV is the dominant softening mechanism below the recrystallization temperature, while a combination of SRV and SRX governs the softening phenomenon beyond this temperature. For the fully-ferritic low carbon steel, the recrystallization temperature is found to be 823 K [55]. Based on the

temperature history during the annealing process shown in Figure 5, the reduction of dislocation density by SRV mechanism can take place throughout the annealing process, while nucleation and growth of fresh grains only occurs beyond 823 K. Therefore, it is important to distinguish the contribution of SRV and SRX in total softening kinetic at every stage of the annealing process.

The progress of total softening (TS) phenomenon over the annealing time can be determined based on the change in the average dislocation density during the annealing process, as follows:

$$X_{TS}^{t} = \frac{\sqrt{\rho_d^0} - \sqrt{\rho_d^t}}{\sqrt{\rho_d^0} - \sqrt{\rho_d^f}} \tag{20}$$

where X_{TS}^{t} is the predicted fraction of TS at annealing time *t*, and ρ_d^0, ρ_d^t and ρ_d^f are the average dislocation density of the as deformed, annealed for a duration of *t*, and fully annealed material, respectively. During the annealing process, the average dislocation density of non-recrystallized regions (ρ_d^{nrx}) gradually decreases due to recovery, while the dislocation density of recrystallized regions drops to a constant value (=10^{11}/m^2) and stays unchanged for the remainder of annealing time. The contribution of static recovery (X_{SRV}^{t}) in fraction of TS (X_{TS}^{t}) can be estimated as below,

$$X_{SRV}^{t} = \frac{\sqrt{\rho_d^0} - \sqrt{\rho_d^{nrx}}}{\sqrt{\rho_d^0} - \sqrt{\rho_d^f}} (1 - V_{SRX}^{t}) \tag{21}$$

where V_{SRX}^{t} is the volume fraction of recrystallized region. Therefore, the contribution of static recrystallization (X_{SRX}^{t}) can be calculated as:

$$X_{SRX}^{t} = \frac{\sqrt{\rho_d^0} - \sqrt{\rho_d^{nrx}}}{\sqrt{\rho_d^0} - \sqrt{\rho_d^f}} V_{SRX}^{t} \tag{22}$$

where the transformation rule of thumb at any annealing time *t*, $X_{SRV}^{t} + X_{SRX}^{t} = X_{TS}^{t}$, is satisfied.

Furthermore, it is important to compare the predicted and experimental kinetics of total softening process to confirm the accuracy of predictions. To that end, the softening fraction of the specimens annealed under different conditions were determined based on the hardness measurements. The experimental fraction of total softening (X_{TS-Exp}^{t}) versus annealing time *t* can be estimated as follows,

$$X_{TS-Exp}^{t} = \frac{H^0 - H^t}{H^0 - H^f} \tag{23}$$

where H^0,H^t, and H^f are the average hardness values for the as received, annealed for a duration of *t*, and fully annealed materials, respectively.

Figure 11 compares the predicted and experimental kinetics of total softening throughout the annealing process for the bulged specimen deformed under path *B* and annealed at T=960 K and a heating rate of h=125 W/m.K, which corresponds to the CA simulation results presented in Figure 7. In this figure, the evolution of X_{TS} as well as its constituents, X_{SRV} and X_{SRX}, over the annealing time is demonstrated. As can be seen, a good agreement between the predicted and experimental X_{TS} is obtained, confirming the validity of the developed model for softening mechanisms. Furthermore, it is clearly observed that the kinetics of softening mechanisms throughout the annealing process could be divided into four stages:

(i) ***No softening***: at the beginning of the annealing process, the specimen at room temperature is exposed to the high temperature annealing environment, resulting in a rapid temperature rise. However, since the temperature throughout this stage is not high enough to overcome the activation energies, no softening mechanism is operative.

(ii) ***SRV only***: the specimen temperature is above the recovery and below the recrystallization temperatures. Therefore, the only softening mechanism operative during this stage is SRV, even though the kinetics of SRV is slow due to the low temperature.

(iii) ***SRV dominant***: both SRV and SRX mechanisms become operative since the temperature is right above the recrystallization temperature. Since the temperature is close to the lower temperature range in which SRX could take place, only some fresh nuclei within the deformed structure forms. Since the volume fraction of recrystallized region is small, it cannot impact the total softening process significantly (according to Eq. (22)). On the other hand, the temperature is high enough to maximize the rate of SRV, that makes SRV as the major contributor for TS progress.

(iv) ***SRX dominant***: further increase in the temperature accelerates the progression of SRX, that includes the formation of fresh crystals and growth toward the deformed context. At this stage, the volume fraction of non-recrystallized region decreases, and the contribution of SRV in TS diminishes according to Eq. (21).

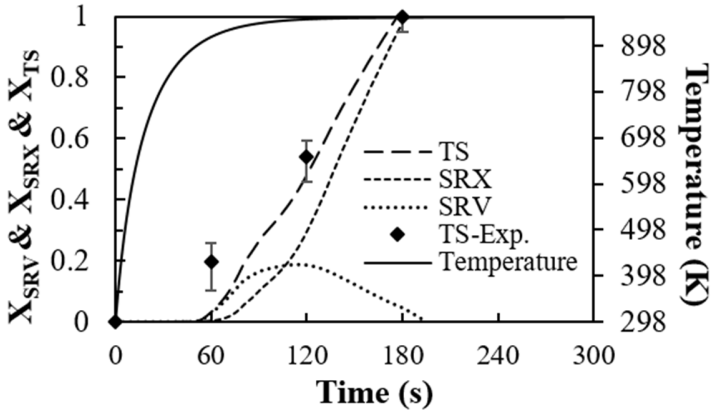

Figure 11: The experimental and numerical softening fraction throughout the annealing of bulged specimen deformed under path *B* and annealed at T=960 K and heating rate of h=125 W/m.K. The individual contributions of recovery and recrystallization in total softening are depicted with dashed lines.

The predicted softening fraction as well as the temporal evolution of microstructure within the bulged tube deformed through path *B* and undergoing annealing at T=960 K and a heating rate of h=20 W/m.K are depicted in Figure 12. By comparing the plots of softening kinetics in this figure to the ones with higher heating rate (h=125 W/m.K) in Figure 11, it can be concluded that the kinetics of SRV, SRX, and TS significantly slow down by reducing the heating rate. In addition, this figure clearly shows the progress of recrystallization that consists of the formation of the fresh nuclei on grain boundaries followed by subsequent grain growth toward the strained region. By

comparing the temporal microstructures to the corresponding kinetics of softening mechanism, it can be realized that the stage (i) of annealing process, where no signs of SRV and SRX is seen, takes the initial 360 seconds of the annealing time. Thereafter, the stage (ii) of the annealing process begins and continues until 480 seconds, where only SRV takes place and the microstructure remains unchanged. The time period between 480 to 630 seconds lies in the stage (iii) of annealing process, in which SRV is the dominant softening mechanism, although some fresh nuclei within the deformed structure is formed. Beyond this stage, the specimen enters the stage (iv) of annealing process, where SRX mechanisms significantly become operative and recrystallized grains conquer the deformed region.

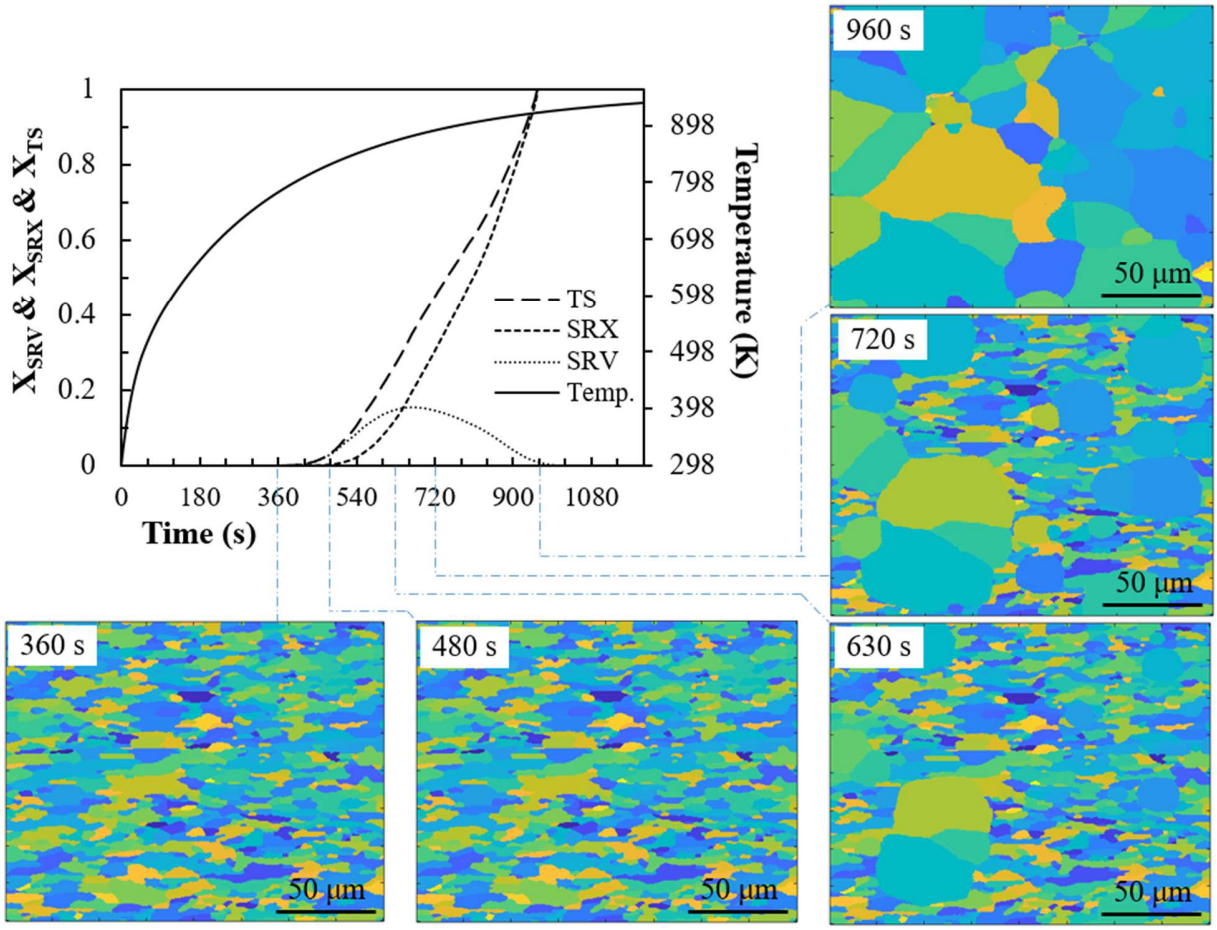

Figure 12: The predicted softening fraction as well as the temporal microstructure evolution throughout the annealing of bulged specimen deformed under path *B* and annealed at T=960 K and a heating rate of h=20 W/m.K.

The final microstructure of the fully recrystallized specimens processed under various deformation and annealing conditions are illustrated in Figure 13. In this figure, the fully recrystallized microstructure predicted by the CA model is compared to the corresponding experimental observations performed by optical microscopy. As can be seen, the predicted grain

topologies are in good agreement with the experimental microstructures for all the specimens. To quantitatively demonstrate this comparison, the corresponding grain size distribution of the microstructures are illustrated in Figure 14. As can be seen, the CA predicted grain size distributions are in complete agreement with the data obtained from the experimental observations. In this regard, an average root mean square error [54] of 2.8 %, 3.5 %, 4.6 % and 4.1 % is calculated between the predicted and experimental grain size distribution data for the fully recrystallized specimens undergoing the deformation and annealing conditions of path *B*: T=960 K-h=98 W/m.K, path *B*: T=960 K-h=20 W/m.K, path *A*: T=960 K-h=125 W/m.K, and path *A*: T=960 K-h=98 W/m.K, respectively.

As observed in Figures 13 and 14, the grain structure of the fully recrystallized specimens undergoing various deformation and annealing conditions becomes significantly coarser when compared to that of the as-deformed specimens illustrated in Figure 6. The corresponding average equivalent grain diameter of the as-deformed and fully recrystallized specimens are tabulated in Table 4. As can be seen, for the specimen deformed through path *A*, the average equivalent grain diameter of the as-deformed specimen is 7.7 μm, which increases to 23 μm for the specimen annealed under the heating rate of h=125 W/m.K. The significant grain coarsening during annealing infers the faster kinetics of grain growth in comparison to the nucleation. In addition, a further increase in the average equivalent grain diameter to 27.1 μm can be seen when the heating rate reduces to h=98 W/m.K, leading to the conclusion that the kinetics of grain growth has an inverse relation with the heating rate. A similar trend can also be seen for the specimen deformed through path *B*, in which the average equivalent grain diameter of the as-deformed specimen (6.2 μm) is increased to 24.3 μm with the reduction of the heating rate to h=20 W/m.K. Note that for the same annealing condition, the average equivalent grain diameter of the specimen deformed through path *B* is lower than that of the specimen deformed through path *A*. This difference can be mainly attributed to the difference in the amount of deformation as shown in Figure 10, where the higher amount of imposed strain in the specimen deformed through path *B* results in a larger number of high energy nucleation sites. This may lead to an accelerated kinetics of nucleation and a refined final recrystallized grain structure.

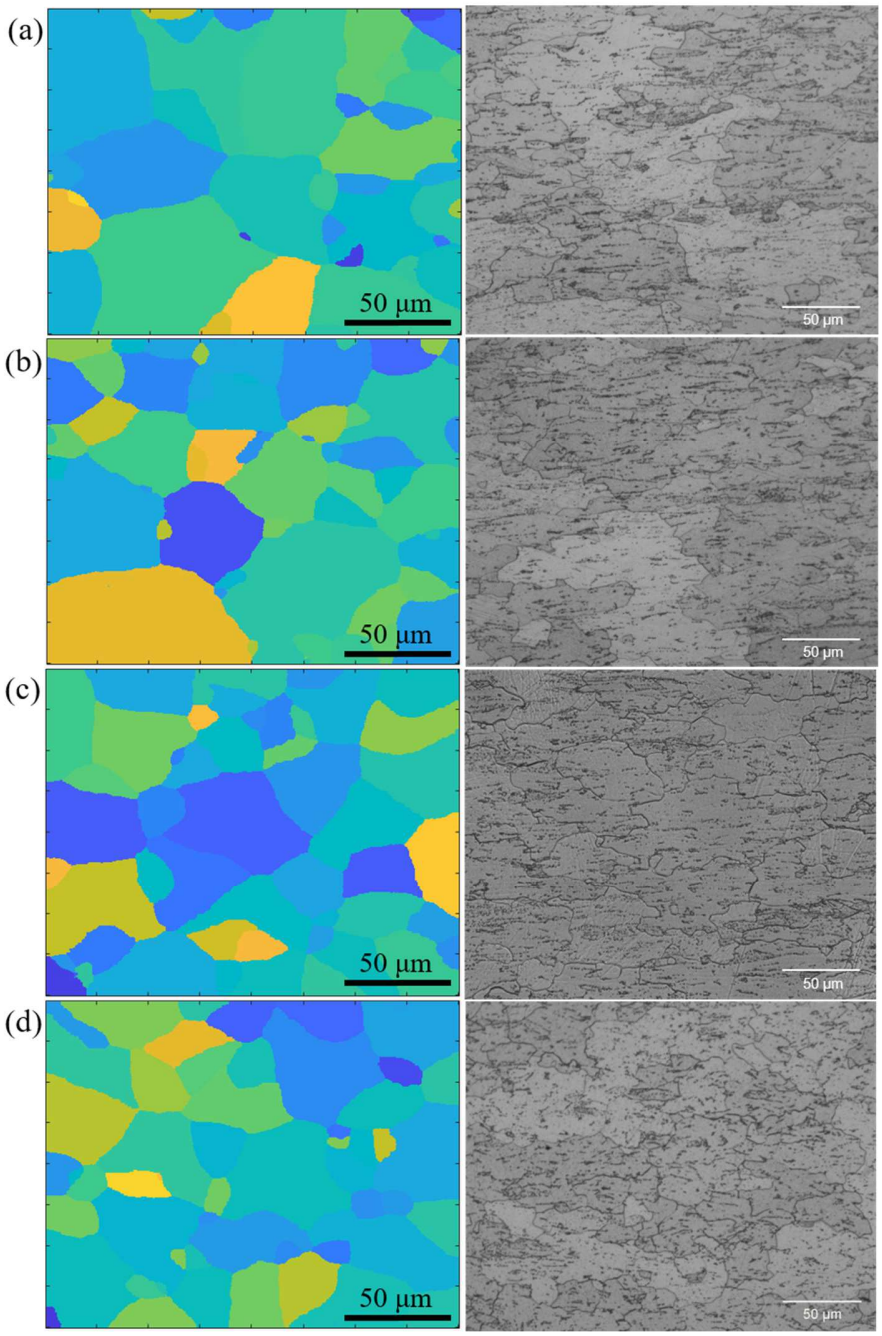

Figure 13: The comparison between the experimental and predicted microstructures of fully recrystallized specimens deformed and annealed under conditions of: (a) path *B*, T=960 K, h=98 W/m.K, (b) path *B*, T=960 K, h=20 W/m.K, (c) path *A*, T=960 K, h=125 W/m.K and (d) path *A*, T=960 K, h=98 W/m.K.

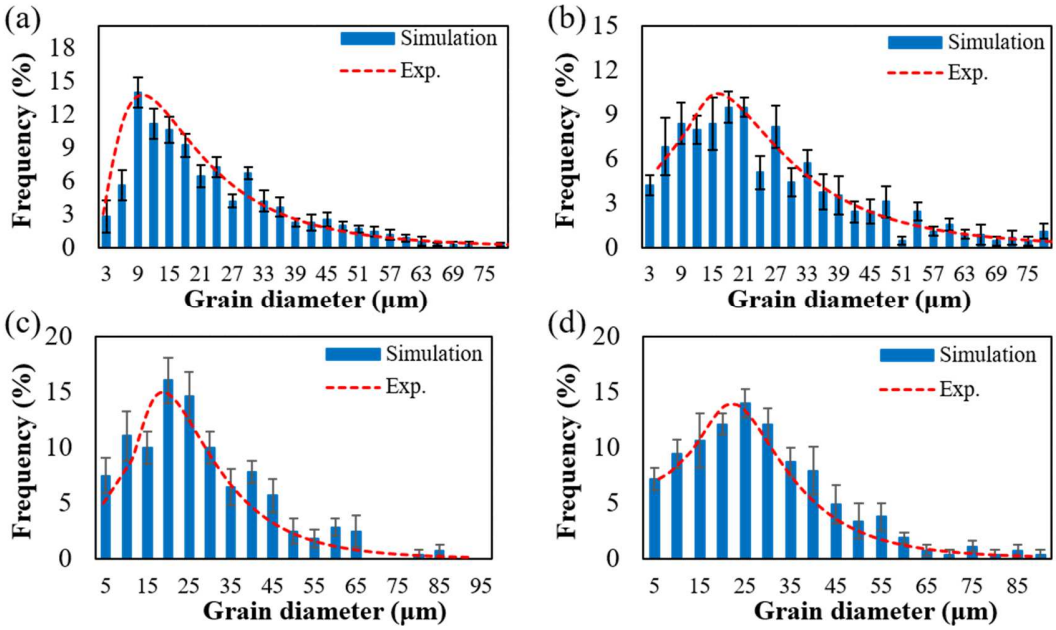

Figure 14: The comparison between the experimental and predicted grain size distributions of fully recrystallized specimens deformed and annealed under conditions of: (a) path *B*, T=960 K, h=98 W/m.K, (b) path *B*, T=960 K, h=20 W/m.K, (c) path *A*, T=960 K, h=125 W/m.K and (d) path *A*, T=960 K, h=98 W/m.K.

Table 4: The average equivalent grain diameter of the fully recrystallized specimens undergoing different deformation and annealing conditions. T= 960 *K* for all the cases.

	Path *A*	Path *B*
as-deformed	7.7 μm	6.2 μm
T= 960 *K*, h=125 W/m.K	23±1.05 μm	10.7±0.6 μm
T= 960 *K*, h=98 W/m.K	27.1±1.1 μm	14.8±0.7 μm
T= 960 *K*, h=20 W/m.K	-	24.3±0.9 μm

5.3. Texture evolution throughout the softening process

To understand the texture evolution within the investigated low carbon steel during the annealing process, the texture data of the as-bulged and annealed samples are compared through collecting EBSD data. The pole figures obtained from the specimen deformed through path *B* and annealed at T=960 K, h=125 W/m.K for different durations are illustrated in Figure 15. The comparison of the pole figure obtained from the as-received tube (Figure 3-b) and the as-deformed material through path *B* (Figure 15-a) shows that the material's texture become more oriented at ND direction on (111) plane during THF process. This texture evolution is consistent with the nature of the performed THF tests, in which the tube is mostly strained at hoop direction as can be seen in Figure 10. Furthermore, Figures 15-b and 15-c illustrate the pole figures of the annealed samples at T=960 K and h=125 W/m.K for 120 second and 180 second, respectively. These pole

figures correspond to the microstructures illustrated in Figure 7-b and -c, which are partially and fully recrystallized, respectively. As seen, the texture evolution throughout the annealing process is not significant, so that the preferred texture is essentially retained while the intensity is slightly changed.

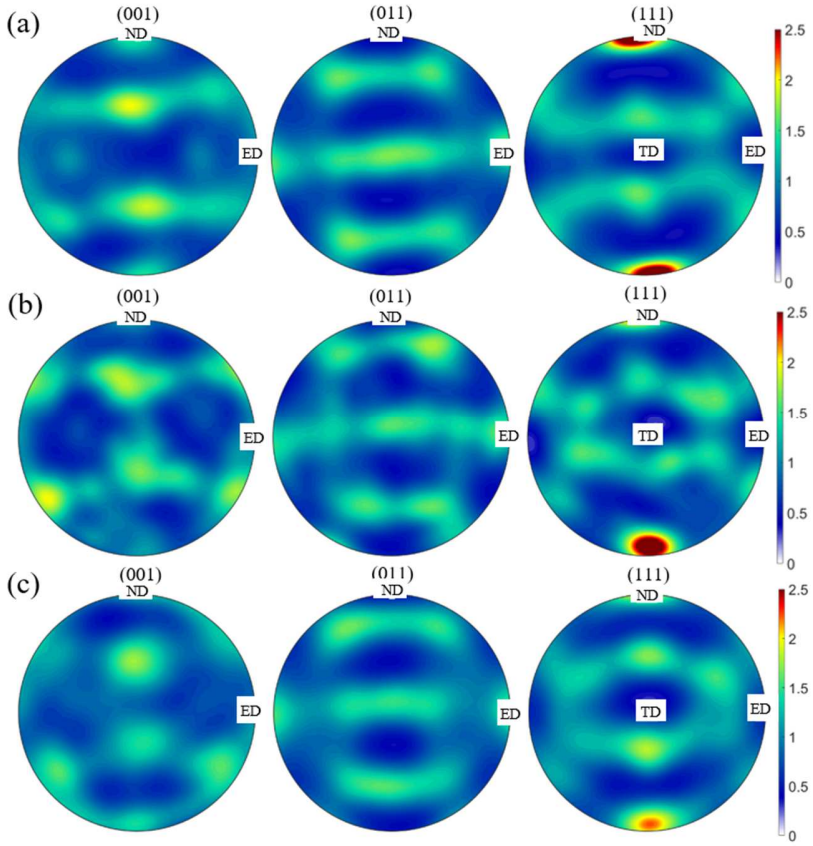

Figure 15: The PFs collected from the hoop cross-section of bulged specimen deformed under path *B* and annealed at T=960 K, h=125 W/m.K, and durations of (a) 0 s, (b) 120 s, and (c) 180 s.

In the present CA model, the recrystallization texture is predicted through an algorithm based on the oriented nucleation theory, in which three different methods are proposed to assign new orientations to the fresh nuclei during the progress of recrystallization. The assigned orientations are reproduced during the subsequent grain growth phenomenon until the recrystallized grains take over the entire microstructure. The comparison between the predicted pole figures through different algorithms for the fully recrystallized specimen deformed under path *B* and annealed at T=960 K, h=125 W/m.K, and t=180 s is shown in Figure 16. By comparing these pole figures to the corresponding experimental pole figure shown in Figure 15-c, it can be realized that the algorithms based on the unchanged orientation (Figure 16-a) and average orientation (Figure 16-

b) could successfully predict the recrystallization texture in the investigated bulged low carbon steel. However, the algorithm based on the random orientation, as shown in Figure 16-c, underestimates the intensity of the orientations, although the preferred orientations are detected.

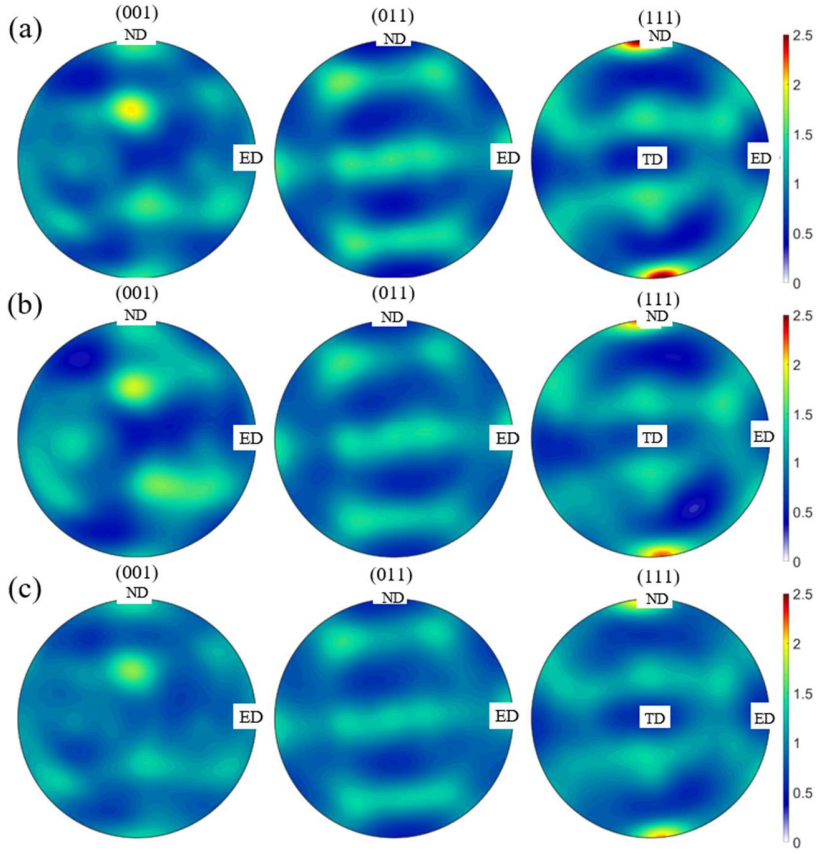

Figure 16: The predicted PFs for the bulged specimen deformed under path *B* and annealed at T=960 K, h=125 W/m.K, and durations of 180 s considering the recrystallization texture algorithms: (a) unchanged orientation, (b) average orientation, and (c) random orientation.

5.4. Development of JMAK model

The predictions attained by the CA model can provide important information to perform further investigations on the SRX behavior of the investigated material. To that end, the time dependent volume fraction of recrystallization (V_{SRX}^{t}) data is extracted from CA simulation results to derive the Johnson-Mehl-Avrami-Kohnogorov (JMAK) analytical model. Figure 17 shows the average V_{SRX} versus annealing time for the specimens undergoing different deformation modes and annealing conditions. As can be seen, like the results shown previously, the increase in the deformation strain and heating rate would accelerate the rate of recrystallization, that is the $V_{SRX} -$

t curves move toward the left of the plot. The $V_{SRX} - t$ curves shown in Figure 17 demonstrate a sigmoid shape, which is compatible with JMAK model as follows [56],

$$V_{SRX}^{t} = 1 - exp(-dt^{n}) \quad (24)$$

where d and n are constants related to grain shape and Avrami exponent, respectively. By taking the logarithm of both sides of this equation, the following relationship is obtained:

$$ln\big(-ln(1 - V_{SRX})\big) = ln(d) + n\, ln(t) \quad (25)$$

where the value of the Avrami exponent n can be determined from the slope of $ln\big(-ln(1 - V_{SRX})\big)$ versus $ln(t)$ plots. By employing the $V_{SRX} - t$ data presented in Figure 17, the representative of the JMAK model using Eqs. (24)-(25) is determined, which is shown in Figure 18. According to this figure, the recrystallization phenomenon can be divided into two regions, among which an abrupt change of the Avrami exponent is seen for all the annealing specimens. A similar behavior has been reported for cold rolled low carbon steel [57]. In the first region, the value of n for the specimens deformed through path A and path B are calculated to be 21.4 and 24.17 for heating rate of 125 W/m.K, and 17.01 and 17.1 for heating rate of 98 W/m.K, respectively. These values of n confirm the high overall rate of SRX at the beginning of recrystallization process, while the recrystallization rate is slightly slower in the specimens annealed under heating rate of 98 W/m.K. Considering the fact that the amount of V_{SRX} at the end of the first region is no more than 0.047 for every specimen, the fast kinetics of nucleation and slow GB movement may cause the high rate of SRX while it keeps V_{SRX} low during this range. Moving toward the second region of recrystallization, the value of n for the specimens deformed through path A and path B are calculated to be 3.55 and 3.62 for heating rate of 125 W/m.K, and 3.49 and 3.53 for heating rate of 98 W/m.K, respectively. In this region, which includes most of the recrystallization process, a significant decrease in the rate of the nucleation and increase in the rate of the GB movement leads to a balanced rate of SRX.

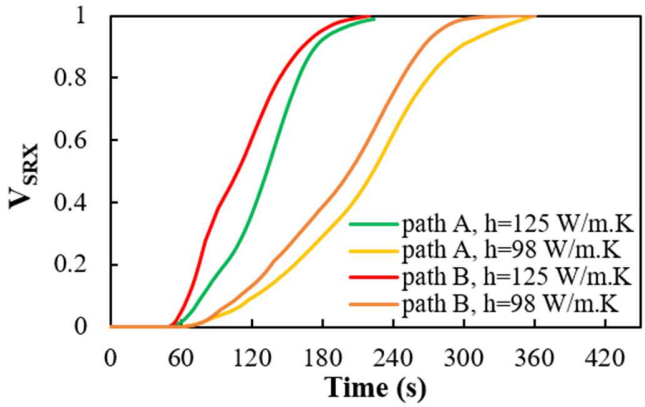

Figure 17: The predicted volume fraction of recrystallization throughout the annealing at T=960 K for different deformation modes and heating rates.

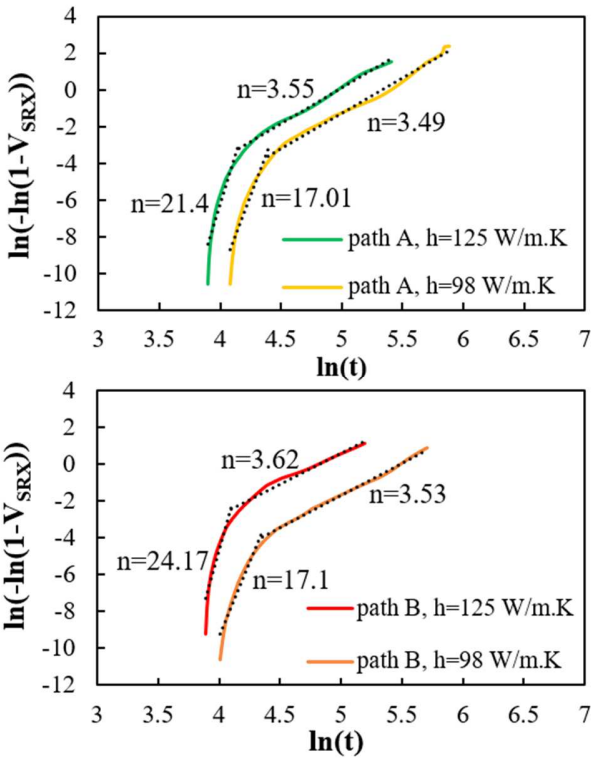

Figure 18: $ln\left(-ln(1-V_{SRX})\right)$ versus $ln(t)$ plots corresponding to the data shown in Figure 17 for derivation of JMAK model.

6. Conclusions

In this study, a hierarchically coupled cellular automata (CA) model, crystal plasticity finite element method (CPFEM), and thermal finite element (FE) model was developed to predict the softening kinetics of a biaxially deformed bulged steel tube during the non-isothermal annealing. Using this model, the kinetics of softening mechanisms including static recovery (SRV) and static recrystallization (SRX) were investigated. Furthermore, the mutual impact of the softening kinetics and recrystallization texture was studied through an algorithm based on oriented nucleation theory. Lastly, the JMAK model based on the data provided by CA simulations was developed to further investigate the SRX behavior. The main results of this study can be concluded as follows,

- The developed CPFEM model successfully predicted the flow characteristics of the bulging tubes. In addition, the hierarchically coupled CA, CPFEM, and thermal FE model successfully predicted the kinetics of softening phenomena during the non-isothermal annealing process under different heating rates. The grain size distribution of the partially and fully annealed specimens undergoing different deformation and annealing conditions were predicted with an average root mean square error of less than 4.6%.
- The grain structure of the fully recrystallized specimens was significantly coarser in comparison to the grain structure of the as-deformed specimen and were negatively correlated with the heating rate.

- The individual contributions of the SRV and SRX in the total softening phenomenon were identified, through which the annealing process was divided into four stages: No softening; SRV only; SRV dominant; and SRX dominant.
- The texture evolution during the progress of recrystallization was well predicted through oriented nucleation theory, in which the preferred as-deformed texture was essentially retained while the intensity was slightly changed.
- The developed JMAK model illustrated that the nucleation was the main operative mechanism during the early stages of SRX while a balanced cooperation of nucleation and grain boundary migration controlled the rest of the SRX phenomenon.

Acknowledgement:
The authors wish to thank the U.S. Department of Energy for the support of this project through the DOE award DOE-FG02-13ER41974 and DOE DE-EE000597, with United States Automotive Materials Partnership LLC (USAMP).

Data availability:

As the data provided in this study forms part of an ongoing study, the raw and processed data required to reproduce these findings cannot be shared at this time.

Appendix A: The established FE model for: A1) thermal FE modeling of bulged specimen during annealing process, and A2) CPFEM simulation of THF process.

A1)

A2)

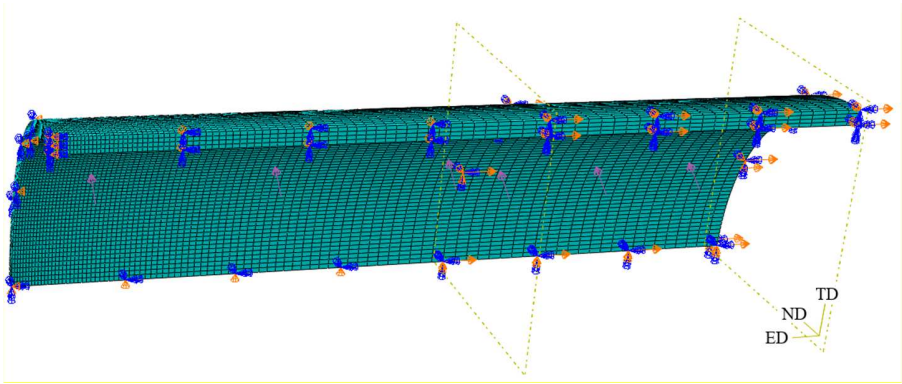

Appendix B: Analytical approach for calculation of principal strain and stress components at the pole of the bulged tube during THF process.

The principal strain and stress components at the pole of the bulged tube throughout THF process can be calculated based on the displacement data measured by DIC technique. By assuming plastic incompressibility and neglecting elastic strains, the instantaneous thickness (t) at the pole of the bulged tube can be calculated as below,

$$t = t_0 exp\big(-(\varepsilon_h + \varepsilon_A)\big) \tag{B1}$$

where t_0 is the initial tube thickness, and ε_h and ε_A are the hoop and axial strain components at the pole of bulged tube, respectively. Then, the stress components in axial and hoop directions at the pole of the bulged tube can be determined, as follows,

$$\sigma_A = \frac{-F_R + \pi R_0^2 P_i}{2\pi R_h t} \tag{B2}$$

$$\sigma_h = \frac{\left(R_A - \frac{t}{2}\right)\left(R_h - \frac{t}{2}\right)P_i - \sigma_A R_h t}{R_A t} \tag{B3}$$

where σ_A and σ_h are axial and hoop stress components, respectively, F_R is the measured reaction force at the end of the tube, P_i is the internal pressure, and R_0 is the initial inside radius of the tube. In addition, R_A and R_h are the radius of the tube in axial and hoop directions at the pole of the bulged tube, respectively, which are determined based on the displacement data obtained from the DIC measurement throughout the THF process. To that end, the equation of a circle is fitted to the coordinates of multiple points on either sides of the pole using the least mean square fitting algorithm [58]. Therefore, the equivalent stress ($\bar{\sigma}$) and equivalent strain ($\bar{\varepsilon}$) at the pole of the bulged tube are determined based on the isotropic von-Mises function, as below,

$$\bar{\sigma} = \sqrt{{\sigma_A}^2 - \sigma_A \sigma_h + {\sigma_h}^2} \tag{B4}$$

$$\bar{\varepsilon} = \frac{2}{\sqrt{3}}\sqrt{({\varepsilon_A}^2 + \varepsilon_A \varepsilon_h + {\varepsilon_h}^2)} \tag{B5}$$

References:

[1] H.W. Hesselbarth, I.R. Göbel, Simulation of recrystallization by cellular automata, Acta Metall. Mater. 39 (1991) 2135–2143. https://doi.org/10.1016/0956-7151(91)90183-2.

[2] C.H.J. Davies, Growth of nuclei in a cellular automaton simulation of recrystallisation, Scr. Mater. 36 (1997) 35–40. https://doi.org/10.1016/S1359-6462(96)00331-4.

[3] R.L. Goetz, V. Seetharaman, Static recrystallization kinetics with homogeneous and heterogeneous nucleation using a cellular automata model, Metall. Mater. Trans. A Phys. Metall. Mater. Sci. 29 (1998) 2307–2321. https://doi.org/10.1007/s11661-998-0108-z.

[4] R.L. Goetz, V. Seetharaman, Modeling dynamic recrystallization using cellular automata, Scr. Mater. 38 (1998) 405–413. https://doi.org/10.1016/S1359-6462(97)00500-9.

[5] K.G.F. Janssens, Random grid, three-dimensional, space-time coupled cellular automata for the simulation of recrystallization and grain growth, Model. Simul. Mater. Sci. Eng. 11 (2003) 157–171. https://doi.org/10.1088/0965-0393/11/2/304.

[6] D. Raabe, L. Hantcherli, 2D cellular automaton simulation of the recrystallization texture of an if sheet steel under consideration of Zener pinning, Comput. Mater. Sci. 34 (2005) 299–313. https://doi.org/10.1016/j.commatsci.2004.12.067.

[7] R.L. Goetz, Particle stimulated nucleation during dynamic recrystallization using a cellular automata model, Scr. Mater. 52 (2005) 851–856. https://doi.org/10.1016/j.scriptamat.2005.01.012.
[8] G. Kugler, R. Turk, Study of the influence of initial microstructure topology on the kinetics of static recrystallization using a cellular automata model, Comput. Mater. Sci. 37 (2006) 284–291. https://doi.org/10.1016/j.commatsci.2005.07.005.
[9] D. Raabe, Introduction of a scalable three-dimensional cellular automaton with a probabilistic switching rule for the discrete mesoscale simulation of recrystallization phenomena, Philos. Mag. A Phys. Condens. Matter, Struct. Defects Mech. Prop. 79 (1999) 2339–2358. https://doi.org/10.1080/01418619908214288.
[10] F. Han, B. Tang, H. Kou, J. Li, Y. Feng, Cellular automata modeling of static recrystallization based on the curvature driven subgrain growth mechanism, J. Mater. Sci. 48 (2013) 7142–7152. https://doi.org/10.1007/s10853-013-7530-3.
[11] N. Yazdipour, C.H.J. Davies, P.D. Hodgson, Microstructural modeling of dynamic recrystallization using irregular cellular automata, Comput. Mater. Sci. 44 (2008) 566–576. https://doi.org/10.1016/j.commatsci.2008.04.027.
[12] Y.C. Lin, Y.X. Liu, M.S. Chen, M.H. Huang, X. Ma, Z.L. Long, Study of static recrystallization behavior in hot deformed Ni-based superalloy using cellular automaton model, Mater. Des. 99 (2016) 107–114. https://doi.org/10.1016/j.matdes.2016.03.050.
[13] C. Huang, X. Jia, Z. Zhang, Modeling and simulation of the static recrystallization of 5754 aluminium alloy by cellular automaton, Metals (Basel). 8 (2018). https://doi.org/10.3390/met8080585.
[14] T. Zhang, S.H. Lu, J. Bin Zhang, Z.F. Li, P. Chen, H. Gong, Y.X. Wu, Modeling of the static recrystallization for 7055 aluminum alloy by cellular automaton, Model. Simul. Mater. Sci. Eng. 25 (2017). https://doi.org/10.1088/1361-651X/aa7121.
[15] C. Schäfer, V. Mohles, G. Gottstein, Modeling of non-isothermal annealing: Interaction of recrystallization, recovery, and precipitation, Acta Mater. 59 (2011) 6574–6587. https://doi.org/10.1016/j.actamat.2011.07.003.
[16] M. Seyed Salehi, S. Serajzadeh, Simulation of static recrystallization in non-isothermal annealing using a coupled cellular automata and finite element model, Comput. Mater. Sci. 53 (2012) 145–152. https://doi.org/10.1016/j.commatsci.2011.09.026.
[17] M.S. Salehi, S. Serajzadeh, Simulation of static softening behavior of an aluminum alloy after cold strip rolling, Comput. Mater. Sci. 69 (2013) 53–61. https://doi.org/10.1016/j.commatsci.2012.11.028.
[18] L. Madej, M. Sitko, K. Radwanski, R. Kuziak, Validation and predictions of coupled finite element and cellular automata model: Influence of the degree of deformation on static recrystallization kinetics case study, Mater. Chem. Phys. 179 (2016) 282–294. https://doi.org/10.1016/j.matchemphys.2016.05.040.
[19] J. Majta, Ł. Madej, D.S. Svyetlichnyy, K. Perzyński, M. Kwiecień, K. Muszka, Modeling of the inhomogeneity of grain refinement during combined metal forming process by finite element and cellular automata methods, Mater. Sci. Eng. A. 671 (2016) 204–213. https://doi.org/10.1016/j.msea.2016.06.052.
[20] D. Raabe, R.C. Becker, Coupling of a crystal plasticity finite-element model with a probabilistic cellular automaton for simulating primary static recrystallization in aluminum, Model. Simul. Mater. Sci. Eng. 8 (2000) 445–462. https://doi.org/10.1088/0965-0393/8/4/304.

[21] C. Zheng, N. Xiao, D. Li, Y. Li, Mesoscopic modeling of austenite static recrystallization in a low carbon steel using a coupled simulation method, Comput. Mater. Sci. 45 (2009) 568–575. https://doi.org/10.1016/j.commatsci.2008.11.021.
[22] W. Chuan, Y. He, L.H. Wei, Modeling of discontinuous dynamic recrystallization of a near-α titanium alloy IMI834 during isothermal hot compression by combining a cellular automaton model with a crystal plasticity finite element method, Comput. Mater. Sci. 79 (2013) 944–959. https://doi.org/https://doi.org/10.1016/j.commatsci.2013.08.004.
[23] E. Popova, Y. Staraselski, A. Brahme, R.K. Mishra, K. Inal, Coupled crystal plasticity - Probabilistic cellular automata approach to model dynamic recrystallization in magnesium alloys, Int. J. Plast. 66 (2015) 85–102. https://doi.org/10.1016/j.ijplas.2014.04.008.
[24] F. Han, B. Tang, H. Kou, L. Cheng, J. Li, Y. Feng, Static recrystallization simulations by coupling cellular automata and crystal plasticity finite element method using a physically based model for nucleation, J. Mater. Sci. 49 (2014) 3253–3267. https://doi.org/10.1007/s10853-014-8031-8.
[25] C. Haase, M. Kühbach, L.A. Barrales-Mora, S.L. Wong, F. Roters, D.A. Molodov, G. Gottstein, Recrystallization behavior of a high-manganese steel: Experiments and simulations, Acta Mater. 100 (2015) 155–168. https://doi.org/10.1016/j.actamat.2015.08.057.
[26] H. Li, X. Sun, H. Yang, A three-dimensional cellular automata-crystal plasticity finite element model for predicting the multiscale interaction among heterogeneous deformation, DRX microstructural evolution and mechanical responses in titanium alloys, Int. J. Plast. 87 (2016) 154–180. https://doi.org/https://doi.org/10.1016/j.ijplas.2016.09.008.
[27] A. Asgharzadeh, S.A. Nazari Tiji, T. Park, J.H. Kim, F. Pourboghrat, Cellular automata modeling of the kinetics of static recrystallization during the post-hydroforming annealing of steel tube, J. Mater. Sci. 55 (2020) 7938–7957. https://doi.org/10.1007/s10853-020-04559-w.
[28] S.A. Nazari Tiji, T. Park, A. Asgharzadeh, H. Kim, M. Athale, J.H. Kim, F. Pourboghrat, Characterization of yield stress surface and strain-rate potential for tubular materials using multiaxial tube expansion test method, Int. J. Plast. (2020) 102838. https://doi.org/https://doi.org/10.1016/j.ijplas.2020.102838.
[29] A. Asgharzadeh, S.A. Nazari Tiji, T. Park, F. Pourboghrat, Non-isothermal Modeling of Static Recrystallization in Hydroformed Steel Tube Using a Coupled Cellular Automata and Finite Element Model, Springer International Publishing, 2021. https://doi.org/10.1007/978-3-030-75381-8_157.
[30] A. Asgharzadeh, S. Serajzadeh, Development of a stream function-upper bound analysis applicable to the process of plate rolling, Multidiscip. Model. Mater. Struct. 12 (2016) 254–274. https://doi.org/10.1108/MMMS-06-2015-0029.
[31] A. Asgharzadeh, S.A. Nazari Tiji, R. Esmaeilpour, T. Park, F. Pourboghrat, Determination of hardness-strength and -flow behavior relationships in bulged aluminum alloys and verification by FE analysis on Rockwell hardness test, Int. J. Adv. Manuf. Technol. 106 (2020) 315–331. https://doi.org/10.1007/s00170-019-04565-6.
[32] S.A. Nazari Tiji, A. Asgharzadeh, T. Park, S.A. Whalen, M. Reza-E-Rabby, M. Eller, F. Pourboghrat, Microstructure and mechanical properties of the AA7075 tube fabricated using shear assisted processing and extrusion (ShAPE), Arch. Civ. Mech. Eng. 21 (2021) 1–10. https://doi.org/10.1007/s43452-021-00179-6.
[33] A.R. Zamiri, F. Pourboghrat, A novel yield function for single crystals based on combined

constraints optimization, Int. J. Plast. 26 (2010) 731–746. https://doi.org/10.1016/j.ijplas.2009.10.004.
[34] B. Mohammed, T. Park, H. Kim, F. Pourboghrat, R. Esmaeilpour, The forming limit curve for multiphase advanced high strength steels based on crystal plasticity finite element modeling, Mater. Sci. Eng. A. 725 (2018) 250–266. https://doi.org/https://doi.org/10.1016/j.msea.2018.04.029.
[35] B. Mohammed, T. Park, F. Pourboghrat, J. Hu, R. Esmaeilpour, F. Abu-Farha, Multiscale crystal plasticity modeling of multiphase advanced high strength steel, Int. J. Solids Struct. 151 (2018) 57–75. https://doi.org/https://doi.org/10.1016/j.ijsolstr.2017.05.007.
[36] T. Park, L.G. Hector, X. Hu, F. Abu-Farha, M.R. Fellinger, H. Kim, R. Esmaeilpour, F. Pourboghrat, Crystal plasticity modeling of 3rd generation multi-phase AHSS with martensitic transformation, Int. J. Plast. 120 (2019) 1–46. https://doi.org/https://doi.org/10.1016/j.ijplas.2019.03.010.
[37] R. Esmaeilpour, H. Kim, T. Park, F. Pourboghrat, Z. Xu, B. Mohammed, F. Abu-Farha, Calibration of Barlat Yld2004-18P yield function using CPFEM and 3D RVE for the simulation of single point incremental forming (SPIF) of 7075-O aluminum sheet, Int. J. Mech. Sci. 145 (2018) 24–41. https://doi.org/https://doi.org/10.1016/j.ijmecsci.2018.05.015.
[38] R. Esmaeilpour, H. Kim, A. Asgharzadeh, S.A. Nazari Tiji, F. Pourboghrat, M. Banu, A. Bansal, A. Taub, Experimental validation of the simulation of single-point incremental forming of AA7075 sheet with Yld2004-18P yield function calibrated with crystal plasticity model, Int. J. Adv. Manuf. Technol. 113 (2021) 2031–2047. https://doi.org/10.1007/s00170-021-06706-2.
[39] HUTCHINSON JW, Elastic- plastic behavior of polycrystalline metals and composites, Proc. R. Soc. London. A. Math. Phys. Sci. 319 (1976) 247–272. https://doi.org/10.1098/rspa.1970.0177.
[40] A. Zamiri, F. Pourboghrat, F. Barlat, An effective computational algorithm for rate-independent crystal plasticity based on a single crystal yield surface with an application to tube hydroforming, Int. J. Plast. 23 (2007) 1126–1147. https://doi.org/https://doi.org/10.1016/j.ijplas.2006.10.012.
[41] I. Iordanova, V. Antonov, Surface oxidation of low carbon steel during laser treatment, its dependence on the initial microstructure and influence on the laser energy absorption, Thin Solid Films. 516 (2008) 7475–7481. https://doi.org/10.1016/j.tsf.2008.03.031.
[42] M. Verdier, Y. Brechet, P. Guyot, Recovery of A1Mg alloys: Flow stress and strain-hardening properties, Acta Mater. 47 (1998) 127–134. https://doi.org/10.1016/S1359-6454(98)00350-4.
[43] F.J. Humphreys, M. Hatherly, Recrystallization of Single-Phase Alloys, in: Recryst. Relat. Annealing Phenom., 2004: pp. 215–IV. https://doi.org/10.1016/b978-008044164-1/50011-6.
[44] S.V.S. Narayana Murty, S. Torizuka, K. Nagai, Ferrite grain size formed by large strain-high Z deformation in a 0.15C steel, Mater. Trans. 46 (2005) 2454–2460. https://doi.org/10.2320/matertrans.46.2454.
[45] S. Shabaniverki, S. Serajzadeh, Simulation of softening kinetics and microstructural events in aluminum alloy subjected to single and multi-pass rolling operations, Appl. Math. Model. 40 (2016) 7571–7582. https://doi.org/10.1016/j.apm.2016.01.060.
[46] M. Matsumoto, T. Nishimura, Mersenne Twister: A 623-Dimensionally Equidistributed

Uniform Pseudo-Random Number Generator, ACM Trans. Model. Comput. Simul. 8 (1998) 3–30. https://doi.org/10.1145/272991.272995.
[47] A. Brahme, J. Fridy, H. Weiland, A.D. Rollett, Modeling texture evolution during recrystallization in aluminum, Model. Simul. Mater. Sci. Eng. 17 (2009). https://doi.org/10.1088/0965-0393/17/1/015005.
[48] G. Gottstein, R. Sebald, Modelling of recrystallization textures, J. Mater. Process. Technol. 117 (2001) 282–287. https://doi.org/10.1016/S0924-0136(01)00781-6.
[49] L. Kestens, J.J. Jonas, Modeling texture change during the static recrystallization of interstitial free steels, Metall. Mater. Trans. A. 27 (1996) 155–164. https://doi.org/10.1007/BF02647756.
[50] F. Bachmann, R. Hielscher, H. Schaeben, Texture analysis with MTEX- Free and open source software toolbox, Solid State Phenom. 160 (2010) 63–68. https://doi.org/10.4028/www.scientific.net/SSP.160.63.
[51] S.A. Kim, W.L. Johnson, Elastic constants and internal friction of martensitic steel, ferritic-pearlitic steel, and α-iron, Mater. Sci. Eng. A. 452–453 (2007) 633–639. https://doi.org/10.1016/j.msea.2006.11.147.
[52] V.N. Serebryanyi, V. V. Mishakin, A. V. Gonchar, Acoustic and X-ray Diffraction Texture Parameters and the Elastic Constants of Low-Carbon Steel before and after Fatigue Tests, Russ. Metall. 2020 (2020) 1142–1146. https://doi.org/10.1134/S0036029520100225.
[53] A. Martínez-de-Guerenu, F. Arizti, I. Gutiérrez, Recovery during annealing in a cold rolled low carbon steel. Part II: Modelling the kinetics, Acta Mater. 52 (2004) 3665–3670. https://doi.org/10.1016/j.actamat.2004.04.020.
[54] A. Asgharzadeh, H. Jamshidi Aval, S. Serajzadeh, A Study on Flow Behavior of AA5086 Over a Wide Range of Temperatures, J. Mater. Eng. Perform. 25 (2016). https://doi.org/10.1007/s11665-016-1927-5.
[55] J.T. Wang, C. Xu, Z.Z. Du, G.Z. Qu, T.G. Langdon, Microstructure and properties of a low-carbon steel processed by equal-channel angular pressing, Mater. Sci. Eng. A. 410–411 (2005) 312–315. https://doi.org/10.1016/j.msea.2005.08.111.
[56] Y. Gu, G. ying Qiao, D. yong Wu, B. Liao, F. ren Xiao, Precipitation kinetics of Nb carbonitride in austenite and acicular ferrite and its effect on hardness of high-Nb steel, Mater. Chem. Phys. 183 (2016) 506–515. https://doi.org/10.1016/j.matchemphys.2016.09.008.
[57] M. Oyarzábal, A. Martínez-de-Guerenu, I. Gutiérrez, Effect of stored energy and recovery on the overall recrystallization kinetics of a cold rolled low carbon steel, Mater. Sci. Eng. A. 485 (2008) 200–209. https://doi.org/10.1016/j.msea.2007.07.077.
[58] W. Gander, G.H. Golub, R. Strebel, Least-squares fitting of circles and ellipses, Bit. 34 (1994) 558–578. https://doi.org/10.1007/BF01934268.